Differential processing and localization of human Nocturnin controls metabolism of mRNA and nicotinamide adenine dinucleotide cofactors

Received for publication, January 10, 2020, and in revised form, August 6, 2020 Published, Papers in Press, August 23, 2020, DOI 10.1074/jbc.RA120.012618

Elizabeth T. Abshire[1,2], Kelsey L. Hughes[1,‡], Rucheng Diao[3,‡], Sarah Pearce[4,5,‡], Shreekara Gopalakrishna[4], Raymond C. Trievel[2], Joanna Rorbach[4,5], Peter L. Freddolino[2,3], and Aaron C. Goldstrohm[1,*]

From the [1]Department of Biochemistry, Molecular Biology, and Biophysics, University of Minnesota, Minneapolis, Minnesota, USA, the Departments of [2]Biological Chemistry and [3]Computational Medicine and Bioinformatics, University of Michigan Medical School, Ann Arbor, Michigan, USA, the [4]Department of Medical Biochemistry and Biophysics, Division of Molecular Metabolism, Karolinska Institute, Solna, Sweden, and the [5]Max Planck Institute Biology of Ageing - Karolinska Institute Laboratory, Karolinska Institute, Stockholm, Sweden

Edited by Ronald C. Wek

Nocturnin (NOCT) is a eukaryotic enzyme that belongs to a superfamily of exoribonucleases, endonucleases, and phosphatases. In this study, we analyze the expression, processing, localization, and cellular functions of human NOCT. We find that NOCT protein is differentially expressed and processed in a cell and tissue type–specific manner to control its localization to the cytoplasm or mitochondrial exterior or interior. The N terminus of NOCT is necessary and sufficient to confer import and processing in the mitochondria. We measured the impact of cytoplasmic NOCT on the transcriptome and observed that it affects mRNA levels of hundreds of genes that are significantly enriched in osteoblast, neuronal, and mitochondrial functions. Recent biochemical data indicate that NOCT dephosphorylates NADP(H) metabolites, and thus we measured the effect of NOCT on these cofactors in cells. We find that NOCT increases NAD(H) and decreases NADP(H) levels in a manner dependent on its intracellular localization. Collectively, our data indicate that NOCT can regulate levels of both mRNAs and NADP(H) cofactors in a manner specified by its location in cells.

Nocturnin (NOCT) is a member of the exonuclease-endonuclease-phosphatase (EEP) superfamily of enzymes and is conserved from insects to vertebrates (1–6). Whereas members of the EEP superfamily act on diverse substrates, ranging from nucleic acids to phospholipids, NOCT is most similar to the CCR4 subclass, which suggested a role in RNA metabolism (1, 2, 6). CCR4 enzymes are exoribonucleases that degrade the 3′ polyadenosine tail of mRNAs (*i.e.* deadenylases) (7). One feature that distinguishes NOCT from other CCR4 enzymes is its unique N terminus, the function of which was unknown (1).

Analysis of knockout mice has established roles for NOCT in cellular differentiation and metabolism. NOCT was first discovered due to its circadian expression pattern (2). Subsequent work indicated that NOCT is not essential for circadian gene expression or behavior (4). Instead, knockout of NOCT results in resistance to high-fat diet–induced obesity. NOCT knockout mice exhibit defects in absorption, transport, and storage of fat (4, 8). In addition, NOCT knockout mice have increased bone mass with reduced bone marrow adiposity, indicating that NOCT negatively regulates osteogenesis while promoting adipogenesis (4, 9, 10). The biological roles of NOCT in humans remain largely unknown, as do its molecular functions.

Given its relationship to CCR4-type deadenylases, past effort has focused on the ability of NOCT to degrade RNA substrates. Initial biochemical assays suggested that NOCT could degrade poly(A) RNA *in vitro*; however, subsequent analyses using pure recombinant NOCT (rNOCT) did not detect cleavage of poly (A) substrate RNAs (1, 2, 11, 12). As only a few RNA substrates have been tested, it remains plausible that NOCT acts on specific RNA substrates and/or requires unknown partners or modifications that were missing from the biochemical assays.

Multiple approaches provide evidence that NOCT acts on mRNAs *in vivo*. First, when directed to a reporter mRNA in tethered function assays, NOCT reduced translation and RNA stability (1). The repressive activity of NOCT depends on the 3′ end of its target mRNA; it can affect poly(A) reporter mRNA but not a derivative with a 3′ triple helix structure (13, 14). Moreover, mutations in conserved residues of the putative active site of NOCT reduced its repressive activity (1). In these aspects, NOCT exhibits mRNA regulatory activity similar to the CCR4-NOT deadenylase complex (7, 15, 16). Further evidence in support of NOCT-mediated mRNA regulation comes from knockout mice or RNAi depletion of NOCT in liver or cultured cells, respectively; loss of NOCT altered gene expression at the transcript level (10, 17–20). The effect of human NOCT on mRNAs remained unexplored; therefore, in this study, we analyzed its impact on the transcriptome in cultured human cells.

The relationship of NOCT to the EEP superfamily suggests that it may also act on other types of phosphorylated substrates.

‡These authors contributed equally to this work.
*For correspondence: Aaron C. Goldstrohm, agoldstr@umn.edu.
Present address for Elizabeth T. Abshire: Dept. of Biochemistry and Biophysics, School of Medicine and Dentistry, University of Rochester, Rochester, New York, USA.
Present address for Kelsey L. Hughes: Macmillan Learning, Austin, Texas, USA.
Present address for Sarah Pearce: Centre for Discovery Brain Sciences, University of Edinburgh, Edinburgh, Scotland, United Kingdom.

Precedent for this hypothesis is illustrated by the CCR4-type deadenylase PDE12, which hydrolyzes the signaling molecule 2′–5′ oligoadenylate, in addition to poly(A) RNA substrates (21–23). We previously analyzed the ability of NOCT to act on a library of phosphorylated nucleotides, sugars, and lipids, none of which were substrates for rNOCT (1). Interestingly, a recent study reported that purified NOCT can remove the 2′ phosphate of the NADPH cofactors NADPH and $NADP^+$ (24).

The intracellular localization of NOCT remains incompletely understood, which affects determination of its molecular function and substrates. Previously, overexpressed NOCT was reported to be either cytoplasmic or perinuclear, whereas endogenous NOCT has been reported to localize to the nucleus or cytoplasm of mouse embryo cells or to the cytoplasm in *Xenopus* retina (2, 9, 25, 26). Intriguingly, sequence analysis of the unique N terminus of mouse and human NOCT detected the presence of a putative mitochondrial targeting sequence (MTS) (Fig. 1*a*) (6). Moreover, NOCT mRNA possesses two potential translation initiation sites, only one of which would include the MTS, although their utilization has not been determined.

In this report, we examined the function and localization of NOCT protein at the levels of mRNA and NAD metabolism. We find that the N terminus of NOCT is necessary and sufficient to confer mitochondrial localization. Our analysis provides evidence for cell– and tissue type–specific control of processing and localization of NOCT protein. By employing a gain-of-function approach with transcriptome-wide quantitation, we observe that the cytoplasmic form of NOCT affects the levels of hundreds of mRNAs. Finally, we observe specific effects of NOCT overexpression on cellular NADPH and $NADP^+$ levels. Together, our data indicate that NOCT can act as a dual-function enzyme that modulates the levels of mRNAs and NADP(H) in a manner specified by its intracellular localization.

Results

Nocturnin protein is post-translationally processed

To analyze NOCT protein expression, we generated an antigen affinity–purified polyclonal antibody. Its specificity was validated by Western blotting in three ways: by detection of 1) overexpressed NOCT (encoding amino acids 1–431) in HEK293 cells and 2) recombinant purified human NOCT(64–431) (Fig. 1*b*) and 3) by RNAi-mediated depletion of endogenous NOCT protein using two different short hairpin RNAs (Fig. S1). In Western blots, this antibody detected two NOCT protein isoforms (Fig. 1*b*). The major NOCT band in the HepG2 liver cell line migrates with an apparent molecular mass of ~55 kDa, which is larger than the predicted 48.2 kDa of full-length, 431-amino acid NOCT (Fig. 1, *a* and *b*). The N terminus of NOCT is highly basic (see below), which may contribute to its reduced electrophoretic mobility. This 55-kDa form of NOCT was not evident in HEK293 cell extract. In both HEK293, and HepG2 cells, a ~41 kDa protein was also detected, albeit with low relative abundance. The presence of two distinct forms of NOCT suggested the potential for differential translation initiation, protein processing, or alternative mRNA processing. Alternative NOCT mRNA isoforms capable of explaining the ~41-kDa product have not been reported in humans; nor did we detect NOCT isoforms in human RNA-Seq data; therefore, we focused on differential translation initiation and/or protein processing.

Examination of the NOCT mRNA suggested the potential for two translation initiation sites: Met-1 and Met-67 (Fig. 1*a*). Translation typically initiates at the first AUG codon (Met-1) within an optimal Kozak sequence context (5′-**GCCRCCAUGG**) (27–29). For NOCT, initiation at Met-1 would produce the full-length 431-amino acid protein. However, the sequence context of NOCT Met-1 (5′-C**CCGGCAUG**U, Kozak consensus match in boldface type) differs from the optimal context, raising the possibility for leaky scanning and initiation at the downstream Met-67 (5′-UGUU**CCAUGG**) (30).

To interrogate use of these initiation sites, we cloned the NOCT cDNA, including its natural 5′ leader sequence and 431-amino acid ORF, into an expression vector. We then mutated either initiation codon from AUG to GGG (M1X or M67G) and transfected the constructs into HEK293 cells. Western blotting analysis indicates that Met-1 is the predominant initiation site, whereas Met-67 is used only if Met-1 is mutated (Fig. 1*b*). Expression of WT NOCT cDNA (residues 1–431) increased the level of the ~41-kDa form. NOCT M1X produced the expected 41.3-kDa NOCT protein, consistent with the scanning mode of translation wherein Met-67 becomes the first AUG codon in this mutant construct. Importantly, the NOCT M67G construct also produced the ~41-kDa protein, indicating that the second AUG is not necessary for production of the ~41-kDa isoform. Together, these observations support the alternate hypothesis that translation of NOCT initiates at Met-1, producing a pre-protein that is processed into the ~41-kDa form.

The N terminus of NOCT contains a putative mitochondrial targeting sequence (MTS) and cleavage site for the mitochondrial processing peptidase (MPP) (Fig. 1*a*) (6, 31). MitoFates and TPpred2 algorithms score the NOCT N terminus MTS probability at 0.94 and 0.98, respectively (31–33). MTS sequences typically reside in the first 90 residues of a protein, form amphipathic helices, have a high arginine content, and contain few negatively charged residues (31). Consistent with these features, amino acids 2–15 of NOCT are predicted to be an amphipathic α-helix within a 74-amino acid polypeptide that has a pI of 12.1 and a dozen arginine residues (6). MitoFates also identified a consensus cleavage site for MPP, including the arginine at the −2-position relative to the cleavage site after Leu-74 (Fig. 1*a*) (31). The resulting NOCT product (aa 75–431, 40.4 kDa) would have a molecular weight consistent with the observed ~41 kDa NOCT band. The MTS in the NOCT pre-protein is predicted to be recognized by the translocase of outer membrane (TOM) resulting in import into the mitochondrial matrix, where it would be cleaved by MPP to produce the ~41-kDa isoform (34).

Deletion of NOCT amino acids 2–15 reduced the MitoFates probability score from 0.94 to 0.035. Consistent with this prediction, deletion of the MTS sequence, NOCTΔ(2–15), abrogated processing of NOCT and resulted in accumulation of a ~55-kDa protein in HEK293 cells (Fig. 1*b*). As expected, the M67G mutation did not alter expression and processing of this

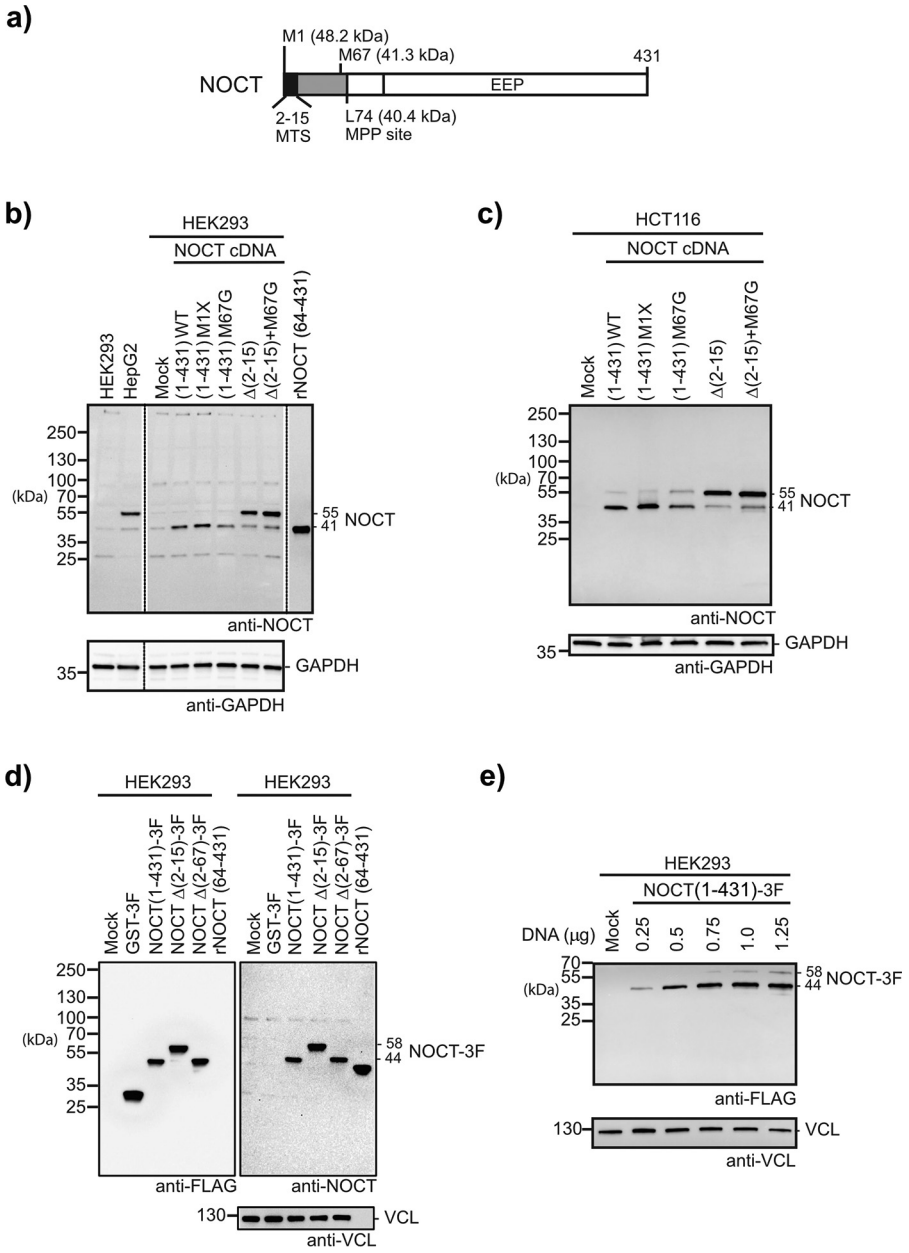

Figure 1. NOCT protein is post-translationally processed in a manner consistent with mitochondrial targeting. *a*, diagram of the NOCT protein-coding sequence. The locations of a predicted MTS and EEP domain are indicated. Two potential translation sites are indicated at the *top* (methionine codons Met-1 and Met-67). The location of a predicted MPP cleavage site, Leu-74, is indicated at the *bottom*. Predicted molecular weights of the resulting NOCT isoforms are indicated. *b*, Western blotting analysis of translation initiation of NOCT protein. Endogenous NOCT protein was detected in cell extracts from human embryonic kidney (HEK293) or human liver (HepG2) cell lines, indicated at the *top*. The apparent molecular weights of endogenous NOCT protein were observed at 41 kDa in HEK293 cells and 55 kDa in HepG2 cells. NOCT protein expression in HEK293 cells was also analyzed in cells transiently transfected with WT NOCT cDNA encoding amino acids 1–431. The role of the two potential initiation sites was tested by mutating the Met-1 AUG codon to GGG (M1X) or the Met-67 AUG codon to a glycine codon, GGG (M67G). The role of the N-terminal predicted MTS in processing of NOCT protein was tested; deletion of the MTS in NOCTΔ(2–15) or NOCTΔ(2–15)+M67G abolishes processing, consistent with mitochondrial localization and processing. *Mock*, untransfected cells. For all Western blots, an equal mass of protein from cell lysates was loaded in each lane of the gel. NOCT protein was detected using Western blotting with antigen affinity–purified, rabbit polyclonal α-NOCT antibody. Purified rNOCT(64–431) served as a positive control for Western blotting detection. Blots were probed using α-GAPDH antibody to assess equivalent loading of the samples. Molecular weight markers in kDa are indicated on the *left*. Apparent molecular weights are indicated on the *right*. The *vertical dashed line* indicates where the blot was cropped to assemble the figure. *c*, same approach as in *b* except using the human colon carcinoma cell line HCT116. *d*, processing of NOCT protein requires the MTS. Shown is expression of NOCT in HEK293 cells from transfected plasmid that expresses the coding sequence fused to C-terminal 3×FLAG epitope tag. NOCT(1–431)-3F is processed to produce a 44-kDa product, including 3 kDa of additional mass from the C-terminal 3×FLAG tag. Deletion of the MTS in NOCTΔ(2–15)-3F results in expression of a 58-kDa form of NOCT-3F, and deletion of amino acids 2–67 resulted in expression of NOCTΔ(2–67)-3F of 44 kDa. An equal mass of protein from cell lysates was analyzed for each sample. NOCT was detected using Western blotting with α-FLAG (*left*) and rabbit α-NOCT (*right*). Western blotting of vinculin using α-VCL assess equivalent loading of the lanes. *e*, detection of processed (44-kDa) and unprocessed (58-kDa) NOCT in HEK293 cells transfected with titration of plasmid expressing full-length NOCT(1–431)-3F in HEK293 cells. The amount of NOCT expression vector is indicated at the *top*. NOCT was detected using Western blotting with rabbit α-FLAG. An equivalent mass of protein from each cell lysate was analyzed in each lane of the gel. Blots were reprobed using α-VCL to assess equivalent loading of the gel lanes.

form of NOCT. Together, these results are consistent with initiation at Met-1 followed by MTS-dependent processing of the ~55-kDa form of NOCT to ~41 kDa. We corroborated these observations in the HCT116 colon cancer cell line (Fig. 1*c*). Interestingly, the processing appears to be cell type–specific, as HepG2 liver cells predominantly produce an unprocessed ~55-kDa form of endogenous NOCT (Fig. 1*b*).

To further examine the processing of NOCT protein, we appended a 3×FLAG (3F) tag to the C terminus of WT NOCT or the deletion of MTS (NOCTΔ(2–15)) or N terminus (NOCTΔ(2–67)) (the 3F tag adds 3 kDa to each protein). Anti-FLAG Western blotting of HEK293 cells shows that full-length NOCT(1–431)-3F was processed to form a ~44-kDa product, whereas deletion of the MTS in NOCTΔ(2–15)-3F prevented processing, resulting in expression of a ~58-kDa product (Fig. 1*d*). A larger deletion of the N-terminal sequence (NOCTΔ(2–67)-3F) produced the expected ~44-kDa product. We also titrated NOCT expression plasmid and observed that, at higher amounts of transfected plasmid, the precursor ~58-kDa form becomes evident, along with the corresponding increase in processed ~44-kDa NOCT (Fig. 1*e*). Taken together, these observations support the efficient processing of NOCT in HEK293 cells, consistent with MTS-dependent mitochondrial import and subsequent proteolytic cleavage by MPP.

Nocturnin is processed and localized to mitochondria in certain cell types

We next examined the localization of NOCT by performing subcellular fractionation of HEK293T cells that were transfected with WT NOCT(1–431)-3F (Fig. 2*a*). Cell homogenates were separated into cytoplasmic and mitochondrial fractions, and NOCT-3F was detected by Western blotting. The ~44-kDa form of NOCT-3F was only detected in the mitochondrial fraction, consistent with MTS-dependent import and processing. As expected, cytosolic uL1 ribosome protein and nuclear histone H3 proteins were not enriched in the mitochondrial fraction. The mitochondrial fractions were subsequently treated with proteinase K to degrade proteins that are outside of intact mitochondria. Under these conditions, outer mitochondrial membrane proteins mitofusin 2 and TOM20 undergo proteolysis due to their exposure to proteinase K, whereas proteins in the mitochondrial matrix (uL4m and uS15m subunits of the mitochondrial ribosome) are protected from proteinase K activity. The ~44-kDa NOCT was also protected from proteolysis, indicating that it is within the mitochondrial membranes. In contrast, disruption of mitochondria with Triton X-100 enabled proteolysis of NOCT, uL4m, and uS15m. Together, our data indicate that NOCT can be localized to mitochondria, where it is imported and processed by MPP.

HepG2 cells predominantly produce the unprocessed ~55-kDa NOCT (Fig. 1*b*). The lack of processing suggests that NOCT may not be imported into the mitochondria and thus is not subject to cleavage by MPP. To examine this further, we fractionated HepG2 cells and performed Western blotting to detect endogenous 55-kDa NOCT, which was predominantly in the mitochondrial fraction (Fig. 2*b*). This mitochondrially associated NOCT is degraded by proteinase K, indicating that it is accessible on the exterior of the

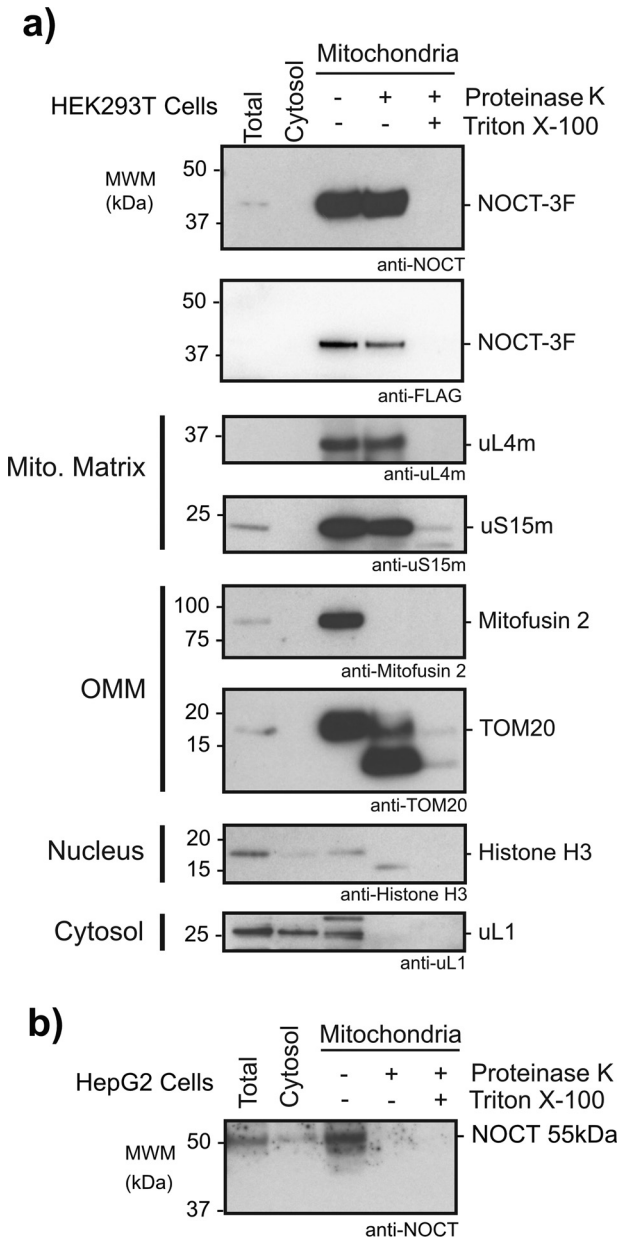

Figure 2. NOCT protein fractionates with mitochondria. *a*, fractionation of HEK293T cells provides evidence that overexpressed NOCT is imported and processed in mitochondria. Shown is Western blotting of subcellular fractions (including total, cytosol, and mitochondria) prepared from HEK293T cells that were transfected with NOCT(1–431)-3F. The mitochondrial fractions were divided into three equal aliquots and were either left untreated, treated with proteinase K, or treated with both proteinase K and Triton X-100. The fractions were then analyzed by SDS-PAGE and Western blotting with the indicated antibodies. NOCT was detected using guinea pig polyclonal anti-NOCT and goat monoclonal anti-DDDDK (FLAG) antibodies. Fractionation was validated using the following antibodies: anti-uL4m and anti-uS15m for the mitochondrial matrix, anti-mitofusin 2 and anti-TOM20 for the outer mitochondrial membrane (*OMM*), anti-histone H3 for the nucleus, and anti-uL1 for the cytoplasm. Apparent molecular weights are indicated on the *right*. *b*, fractionation of HepG2 cells shows that endogenous 55-kDa NOCT is located in the cytosol and exterior of the mitochondria, where it is susceptible to degradation by proteinase K. Western blotting of the indicated fractions from HepG2 cells was performed using anti-NOCT antibody.

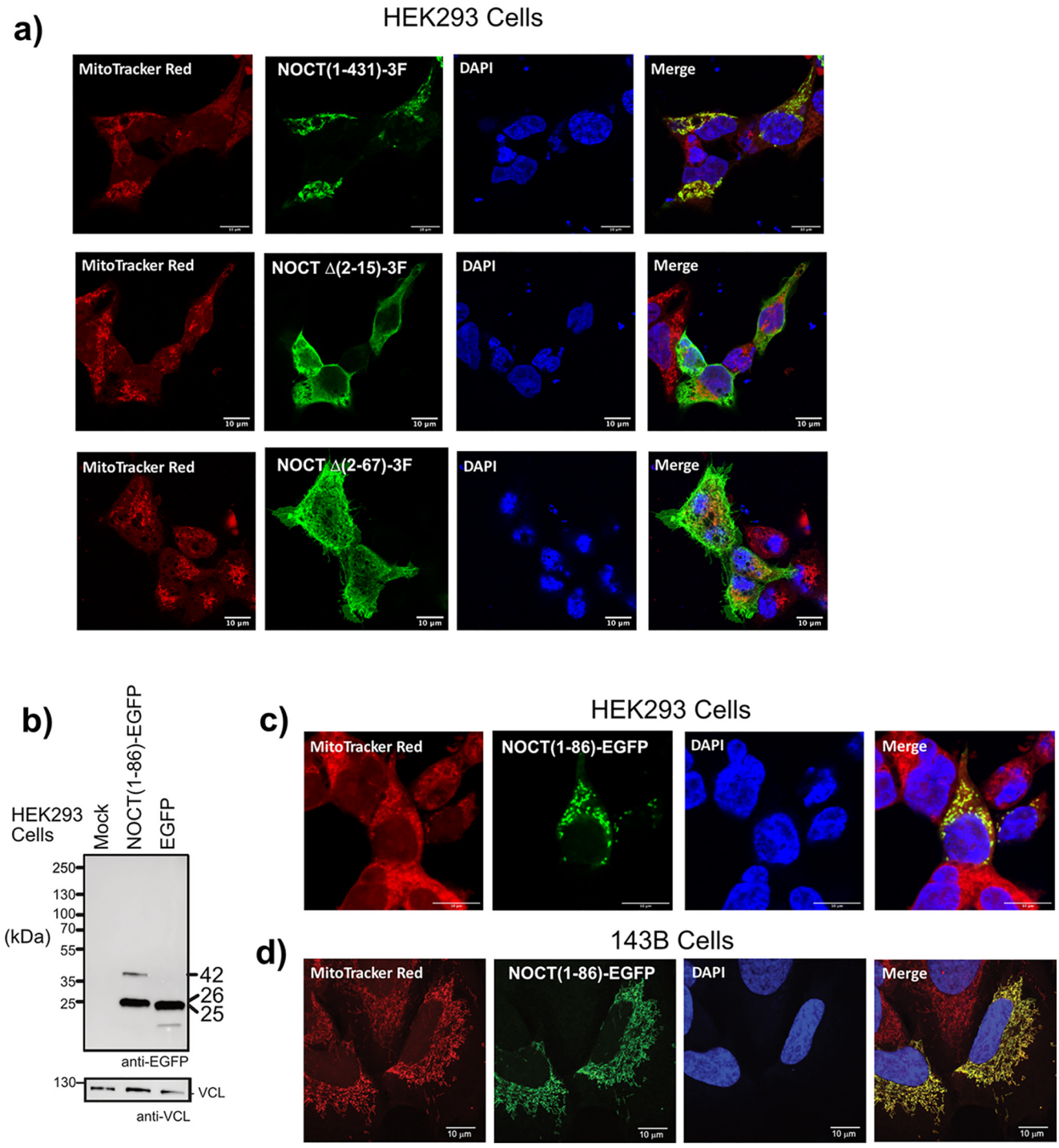

Figure 3. The N terminus of NOCT is necessary and sufficient for processing and mitochondrial localization. *a*, immunofluorescence analysis of intracellular localization of NOCT constructs in HEK293 human cell line. NOCT(1–431)-3F is localized to the mitochondria, whereas NOCTΔ(2–15)-3F and NOCTΔ(2–67)-3F constructs, which lack the MTS, are predominantly localized to the cytoplasm. The indicated NOCT expression plasmids were transfected into HepG2 cells and visualized using anti-FLAG mAb immunofluorescence against the C-terminal 3×FLAG epitope on each construct with Alexa Fluor Plus 488 secondary antibody (*green*). Mitochondria are visualized with MitoTracker Red CMXRos (*red*), and nuclei are visualized with DAPI (*blue*). *White scale bar*, 10 μm. Western blotting of the NOCT proteins is shown in Fig. S2*a* and verifies their expression and processing. *b*, the N terminus of NOCT is sufficient to confer protein processing consistent with mitochondrial localization. The N-terminal 86 amino acids of NOCT were fused to the N terminus of EGFP to create the NOCT(1–86) EGFP expression construct, which was then transfected into HEK293 cells. Cells transfected with the EGFP construct served as a control. Equal amounts of cell lysates were then analyzed by SDS-PAGE and Western blotting using anti-EGFP antibody or, as a loading control, anti-VCL. Molecular weight markers in kDa are indicated on the *left*. Apparent molecular weights are indicated on the *right*. *c* and *d*, NOCT(1–86) EGFP protein (*green*) is localized to the mitochondria in HEK293 cells (*c*) or 143B cells (*d*). Mitochondria are visualized with MitoTracker (*red*), and nuclei are visualized with DAPI (*blue*). *White scale bar*, 10 μm.

mitochondria. Additional 55-kDa NOCT is observed in the cytoplasmic fraction. Thus, HepG2 cells have a pool of unprocessed NOCT that is located on the exterior of mitochondria and in the cytosol. These results suggest that an unknown mechanism may negatively regulate the import of NOCT into the mitochondria in this cell type.

We then performed immunofluorescence to directly visualize the localization of NOCT. First, HEK293 cells were transfected with the FLAG-tagged NOCT constructs (Fig. 3*a*). NOCT was detected using anti-FLAG immunofluorescence in cells that were also stained with MitoTracker and DAPI dyes to visualize mitochondria and nuclei, respectively. NOCT(1–431)-3F overlapped with the MitoTracker stain, indicating localization of NOCT to mitochondria (Fig. 3*a*, *Merge*). To determine whether localization depends on the MTS, we tested the NOCTΔ(2–15)-3F construct, which prevented the mitochondrial localization, as the staining of this construct was diffuse and cytoplasmic (Fig. 3*a*). Likewise, NOCTΔ(2–67)-3F was also observed throughout the cytoplasm. These data indicate that WT NOCT is localized to the mitochondria in HEK293 cells dependent on the N-terminal MTS. Expression and MTS-dependent processing of NOCT-3F protein were verified by Western blotting (Fig. S2*a*). Identical, corroborating observations were made in the human osteosarcoma cell line, 143B (Fig. S3).

To ascertain whether the N terminus of NOCT is sufficient to confer mitochondrial localization and processing, we fused the first 86 amino acids of the NOCT N terminus (containing the MTS in the arginine-rich, basic context and the MPP cleavage site) to EGFP and expressed the construct in HEK293 cells. A minor ~42 kDa band was detected, which is larger than the predicted 35.7 kDa of the NOCT(1–86)-EGFP pre-protein, likely due to the highly basic nature of the N terminus (Fig. 3*b*). A major ~26 kDa band was also produced, consistent with MPP-mediated cleavage of the NOCT presequence (predicted molecular mass 27.9 kDa), and slightly larger than the ~25-kDa EGFP protein, due to the additional 12 amino acids remaining after MPP cleavage. We then used fluorescence microscopy to localize NOCT(1–86)-EGFP and observed that it colocalized with MitoTracker stain in HEK293 cells (Fig. 3*c*). We also confirmed localization of NOCT(1–86)-EGFP in the well-defined mitochondrial network of 143B cells (Fig. 3*d*). Together, our data indicate that the NOCT N-terminal 86 amino acids are sufficient for localization and processing of EGFP fusion protein in the mitochondria.

Having observed that NOCT protein is differentially processed in HEK293 relative to HepG2 cells (Figs. 1 and 2), we hypothesized that processing of NOCT may be regulated in a cell type–specific manner. We followed up on these observations by performing immunofluorescence imaging; however, because our anti-NOCT antibody did not work for immunofluorescence, we instead imaged overexpressed NOCT-3F in HepG2 cells. Interestingly, NOCT(1–431)-3F localized to mitochondria in an MTS-dependent manner (Fig. S2*b*). Western blotting of NOCT(1–431)-3F detected both a minor 58-kDa form and a major 44-kDa form in HepG2 cells (Fig. S2*a*). Thus, HepG2 cells are capable of mitochondrial import/processing of overexpressed NOCT. As expected, deletion of the MTS abrogated processing of NOCT (NOCTΔ(2–15) and NOCTΔ(2–67)). The production of processed 44-kDa NOCT-3F is consistent with its observed mitochondrial localization in HepG2 cells (Fig. S2*b*). These results suggest that overexpressed NOCT-3F may overwhelm/outcompete the unknown regulatory mechanism that prevents processing of endogenous NOCT in HepG2 cells, enabling its mitochondrial import and processing.

Nocturnin protein is expressed and processed in a tissue-specific manner

The expression pattern of NOCT in human tissues has not been investigated in detail; therefore, we assessed available RNA-Seq data, which indicate broad expression of NOCT mRNA in human tissues (Fig. S4). Human NOCT mRNA is most abundant in adipose, breast, liver, lung, muscle, kidney, and certain regions of the brain (*e.g.* cerebellum, frontal cortex), whereas NOCT expression is lowest in ovary, pancreas, bladder, and other brain regions (*e.g.* spinal cord, amygdala, basal ganglia).

To examine the extent to which processing of NOCT is tissue-specific, we performed Western blot analyses on a collection of human tissues using our anti-NOCT antibody (Fig. 4*a*). The ~55-kDa NOCT protein was detected in human brain, kidney, and liver, indicating that full-length, unprocessed NOCT is expressed in multiple tissue types. Of note, the existence of ~55-kDa NOCT in the liver is consistent with that observed in the HepG2 liver cell line (Fig. 1*b*). Several other NOCT species were also observed, including a band at ~40 kDa in brain, skeletal muscle, and, to a lesser degree, heart, suggesting that those tissues can process the NOCT in a manner consistent with mitochondrial localization and MPP-mediated cleavage. We note that additional bands were detected at ~80 kDa in the brain and ~16 kDa in the small intestine; however, the nature of these bands cannot currently be accounted for, and they may result from cross-reaction of the anti-NOCT antibody.

For comparison, we investigated NOCT protein expression in mouse tissues (Fig. 4*b*). The RefSeq-annotated mRNA encoding full-length murine NOCT protein (aa 1–429) is expected to produce a 48-kDa protein with an N-terminal MTS (aa 2–15) and MPP cleavage site (Leu-72) embedded in a presequence with 11 arginines and a pI of 12.2 (MitoFates $p = 0.73$). We therefore expect to observe that murine NOCT is processed similarly to the human enzyme. Indeed, a ~55 kDa NOCT band is observed in brain, lung, and stomach, whereas a major ~40 kDa band was detected in brain, heart, and skeletal muscle and may correspond to MPP-processed NOCT. An additional ~48 kDa band is also detected in brain, heart, small intestine, kidney, liver, spleen, testis (Fig. 4*b*). We note that a second mouse NOCT mRNA isoform (RefSeq XM_006500956.1) encodes a 372-aa protein (42.2 kDa) (XP_006501019). Transcription of this alternative mRNA isoform initiates within intron 1 of the NOCT gene and produces an mRNA with a unique 5′ exon that encodes an alternative 4 amino acids (MALP) in place of the first 61 amino acids normally encoded within exon 1. The ~48 kDa band therefore may represent NOCT translated from this mRNA transcript (Fig. 4*b*). Additional anti-NOCT-reactive ~66, ~80, and ~97 kDa bands are detected in the brain and small intestine but cannot be accounted for by documented transcripts. In summary, these observations indicate that NOCT is differentially expressed and processed in a tissue-dependent manner *in vivo*, with processing consistent with cytoplasmic NOCT localization in human liver and kidney and mitochondrial localization in muscle tissue.

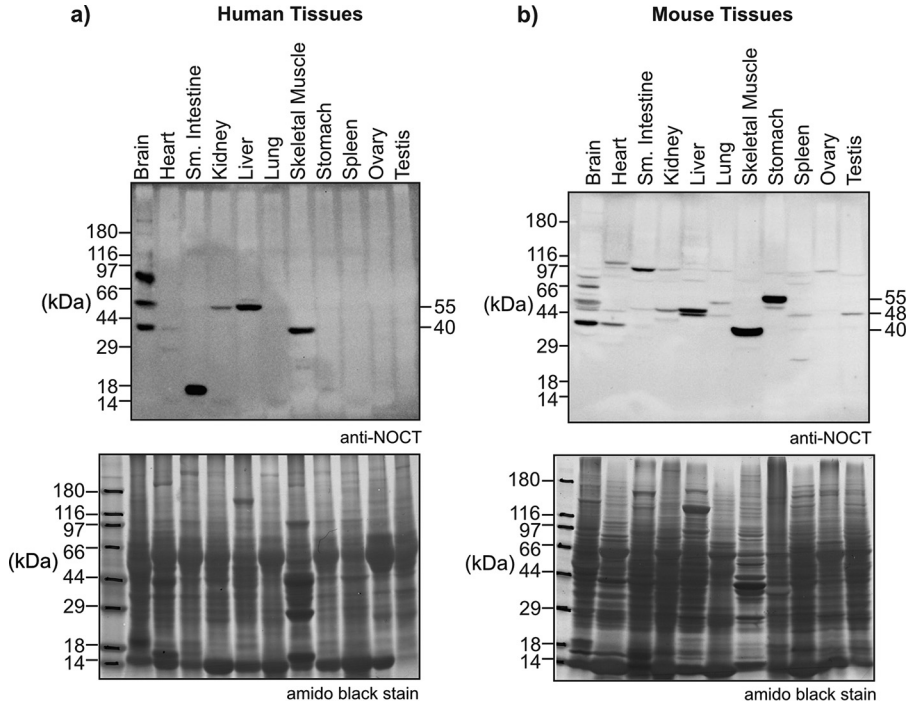

Figure 4. NOCT protein is differentially expressed in human and mouse tissues. Western blotting of human (*a*) and mouse (*b*) tissues, indicated at the *top*, was performed using rabbit polyclonal anti-NOCT antibody. Commercially produced tissue blots contain 50 μg of each tissue. Bands in the 40–55 kDa range are considered feasible to be NOCT. Molecular weight markers are indicated on the *left*. Apparent molecular weights of NOCT bands detected in human brain, heart, kidney, liver, and skeletal muscle and in mouse brain, heart, kidney, liver, lung, skeletal muscle, stomach, spleen, and testis are indicated on the *right*. Each membrane was stained with amido black prior to Western blotting to assess protein content of each tissue sample and detect the molecular weight markers, as shown in the *bottom panels*.

Impact of cytoplasmic Nocturnin on the transcriptome

We next investigated the effect of the cytoplasmic NOCT on the transcriptome. To do so, we used a gain-of-function approach in HEK293 cells, which was advantageous because these cells express a low level of endogenous, processed ~41-kDa NOCT (Fig. 1*b*). It is noteworthy that the HEK293 cell line has characteristics of kidney, adrenal, and neuronal tissues (35, 36). We generated HEK293 clonal lines that stably overexpress NOCTΔ(2–15)-3F construct, which lacks the MTS and is localized to the cytoplasm (Fig. 3*a*). As a negative control, we also generated cells that stably express GSH S-transferase-3×FLAG (GST-3F). Three independent clonal cell lines were generated for each construct and served as biological replicates (Fig. 5*a*). It is important to note that we also attempted to analyze loss of function of NOCT in multiple cell lines. However, we were unable to obtain viable clonal lines with homozygous knockout; nor were we able to achieve sustained depletion of NOCT by RNAi. Due to these technical issues, we focused on the gain of function approach described here. This strategy mimics the induction of NOCT expression by circadian inputs, mitogens, lipids, or other stimuli (4, 8, 11, 37, 38).

To analyze changes in RNA abundances induced by cytoplasmic NOCT, total RNA was isolated from each cell line, rRNA was depleted, and then stranded, whole-transcriptome RNA-Seq was performed. The resulting data measured 21,486 features in the three replicates for each of the different cell lines, including 21,419 Ensembl genes and 67 custom features like overexpression ORFs and ERCC spike-ins. Using stringent statistical significance thresholds (FDR-adjusted p value ≤ 0.05) for expression changes, we identified 490 genes that are significantly affected by NOCT overexpression, with $\log_2$ -fold changes ranging from −2.97 to 2.94 (Fig. 5*b*). As expected, *NOCT*Δ(2–15)-3F mRNA was overexpressed by 3.1-fold. NOCTΔ(2–15)-3F significantly decreased expression of 235 genes relative to the control cells, including 31 genes that were down-regulated between 2- and 4-fold and seven genes down-regulated by more than 4-fold (Fig. 5*c*). Another 255 were significantly up-regulated by NOCTΔ(2–15)-3F, with increased levels of 32 genes between 2- and 4-fold and two genes with a >4-fold increase. Table S1 provides the complete RNA-Seq data set with statistical parameters.

We corroborated the RNA-Seq measurements by measuring changes in levels of select mRNAs using reverse transcription coupled with quantitative PCR (RT-qPCR) (Fig. 5*d*). For this approach, total RNA was independently purified without rRNA depletion. For reverse transcription, random priming was used to avoid potential bias from altered polyadenylation status. First, we confirmed the degree of *NOCT* mRNA overexpression and observed a 2.9-fold increase, consistent with the 3.1-fold increase measured by RNA-Seq. Next, we measured the change in expression of five of the top 10 down-regulated mRNAs (highlighted in Fig. 5*c*). *DLGAP1* encodes a neuron-specific component of the scaffold for glutamate receptors (39). *RORB* encodes a nuclear hormone receptor that regulates brain development and bone formation (40, 41). *TMEFF2* is a neuronal transmembrane protein linked to multiple cancers (42). *PTPRZ1* is a brain-specific protein that regulates neuronal development and cell migration (43). *FRRS1L* is part of the neuronal AMPA receptor and is linked to infantile epileptic encephalopathy and

intellectual disability (44, 45). For each transcript, the log-fold change measurements with RT-qPCR were concordant with the RNA-Seq data (Fig. 5d). We also confirmed that three mRNAs (*B2M*, *ACTB*, and *TBP*) were not affected by NOCT overexpression as measured by both RNA-Seq and RT-qPCR. Thus, two independent assays confirm that cytoplasmic NOCT can significantly change expression of specific genes.

We performed information-theoretic pathway analysis using iPAGE (46) to identify gene ontology (GO) terms that are either

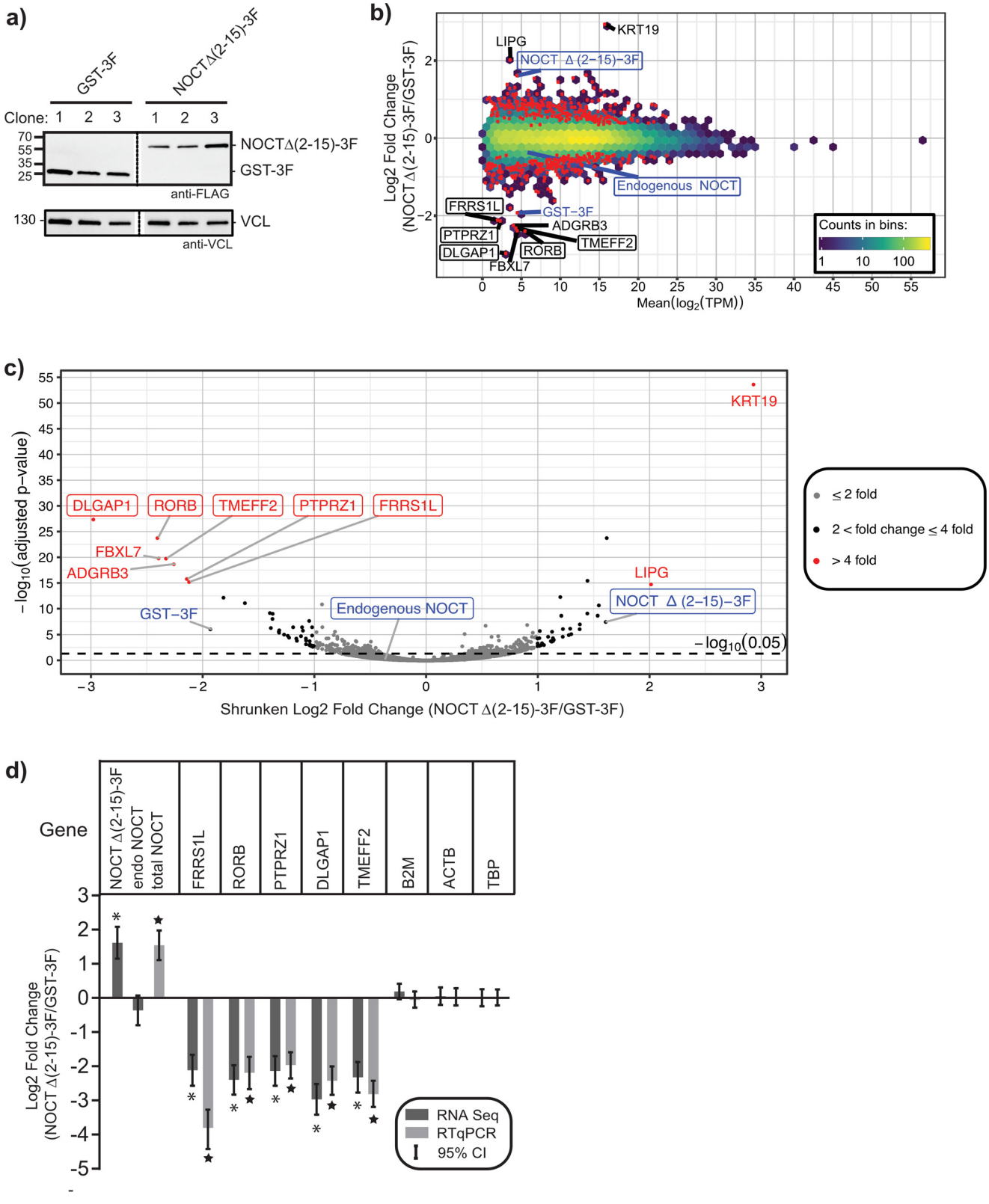

significantly over- or underrepresented in the set of genes affected by NOCTΔ(2–15)-3F in our RNA-Seq data set (Fig. 6). iPAGE permits identification of GO terms that have significant mutual information with the expression profile, thus identifying pathways that are significantly affected by NOCT overexpression. We primarily focused on overrepresented GO terms in the down-regulated genes because these are the most likely to be repressed by NOCT, including negative regulation of osteoblast differentiation (GO:0045668) and fatty acid metabolic process (GO:0006631). These categories are intriguing because NOCT was reported to negatively regulate osteoblastogenesis and bone density and to promote adipogenesis (4, 9, 10, 47). Figs. S5–S8 provide examples of gene-level, $\log_2$ -fold changes for select GO terms that are informative based on iPAGE analysis, including those pertaining to bone development, mitochondrial function, NAD metabolism, and neuronal functions. Each of these GO terms, as listed in Fig. 6, is significantly informative as assessed by permutation-based tests with iPAGE (46).

Among the significantly enriched GO terms identified by iPAGE, several are relevant to mitochondrial components and processes, including mitochondrial respiratory chain complex I (GO:0005747) and mitochondrion organization (GO:0007005), suggesting that cytoplasmic NOCT can regulate expression of mitochondrial proteins (Fig. 6 and Fig. S6). We also observed enriched GO terms linked to NAD cofactor functions, including NADH dehydrogenase (ubiquinone) activity (GO:0008137) (Fig. 6 and Fig. S7).

Multiple GO terms associated with neuronal functions were significantly enriched in NOCT-affected genes, including neuropeptide signaling pathway (GO:0007218), neural tube closure (GO:0001843), and potassium channel activity (GO:0005267) (Fig. 6 and Fig. S8). The latter term includes significantly reduced *KCNQ5*, *KCNA4*, *KCNV1*, *KCND3*, *KCNT2*, and *KCNQ2* genes, which encode neuronal voltage-gated potassium channels that are linked to intellectual disability, microcephaly, seizures, and movement disorders (48, 49). The data indicate that NOCT can down-regulate transcripts that encode proteins with neuronal functions.

Nocturnin affects cellular levels of NADH cofactors

Purified NOCT was recently reported to dephosphorylate the metabolites $NADP^+$ and NADPH in biochemical assays (25). We therefore sought to analyze the effect of differentially localized NOCT on these metabolites in live cells. We predicted that NOCT phosphatase activity may decrease levels of NADP(H) and increase the levels of cellular NAD(H). To assess NOCT-mediated changes in metabolite levels, we created HEK293-derived cell lines with stably integrated, doxycycline (Dox)-inducible NOCT, including mitochondrial localized NOCT(1–431)-3F or cytoplasmic NOCTΔ(2–15)-3F. Three clonal cell lines were created for each construct, and matched WT cell lines were used as negative controls. Dox treatment induced the anticipated ~58-kDa NOCTΔ(2–15)-3F protein (Fig. 7*a*). Likewise, Dox-induced NOCT(1–431)-3F was processed to the ~44-kDa form (Fig. 7*b*). We also measured induction of each NOCT construct by RT-qPCR and observed 14- and 4.2-fold induction of NOCTΔ(2–15)-3F and NOCT (1–431)-3F, respectively (Fig. 7*c*). Next, we measured the effect of induced NOCT on the relative levels of NAD^+, NADH, $NADP^+$, and NADPH in each cell line using luminescence-coupled assays. To assess reproducibility, we performed three independent experiments, each with three biological replicates for each condition. The -fold change of NAD metabolites was then calculated between the Dox-induced state and the noninduced, vehicle-treated state (Fig. 7*d*). We applied a Bayesian statistical analysis of the resulting data to assess reproducibility and significance.

The resulting data demonstrate that NOCTΔ(2–15)-3F significantly increased the levels of NAD^+ and NADH. These results suggest that cytoplasmic NOCT can dephosphorylate NADP(H) to increase the level of NAD^+/NADH. However, NOCTΔ(2–15)-3F did not significantly reduce the pool of either $NADP^+$ or NADPH relative to control cells. Induced NOCT(1–431)-3F significantly reduced the levels of $NADP^+$ and NADPH, indicating that when localized to the mitochondria, NOCT can dephosphorylate $NADP^+$ and NADPH. The pool of NAD^+ and NADH was not detectably changed by mitochondrial NOCT. Together, these results provide evidence that NOCT can alter NAD metabolite levels in a manner dependent on its intracellular localization. We also investigated the potential impact of NOCT on overall ATP levels and observed that neither cytoplasmic NOCTΔ(2–15)-3F nor mitochondrial NOCT(1–431)-3F affected ATP levels. Therefore, NOCT overexpression does

Figure 5. Impact of cytoplasmic NOCTΔ(2–15)-3F on the transcriptome. *a*, GST-3F or NOCTΔ(2–15)-3F proteins were stably transfected and expressed in three separate clonal HEK293 cell lines, as assessed by Western blotting of equal mass of each cell extract using α-FLAG. Western blotting detection of VCL confirmed equivalent loading of the gel lanes. The *vertical dashed line* indicates where the blot was cropped to assemble the figure. *b*, differential gene expression was measured by performing RNA-Seq on rRNA-depleted RNA isolated from the three clonal HEK293 cell lines that overexpressed NOCTΔ(2–15)-3F relative to the three negative control HEK293 cell lines that expressed GST-3F. Gene expression changes were analyzed using DESeq2. $\log_2$ -fold changes of gene expression were plotted versus the $\log_2$ average relative expression level of all six samples, measured in TPM. The *scaled color* shows the counts of genes in each hex-bin. *Red points* indicate genes with significant changes in gene expression by an adjusted *p* value threshold of 0.05. The *black labels* indicate genes with expression changes ≥4-fold. In *b* and *c*, *blue labels* point to the values for overexpressed NOCTΔ(2–15)-3F and the endogenous NOCT, and the *labeled boxes* indicate genes for which we obtained qPCR validation. *c*, volcano plot comparing statistical significance of measurements *versus* the $\log_2$ -fold change in gene expression between NOCTΔ(2–15)-3F and GST-3F conditions. The *red points* and *labels* show the genes that have a ≥4-fold change, whereas *black points* are for genes with <4-fold changes but ≥2-fold changes, and *gray points* are for genes with <2-fold changes. *Dashed line*, FDR-corrected *p* value threshold of 0.05. All data and statistics for the RNA-Seq analysis are reported in Table S1. *d*, corroboration of NOCT-mediated regulation of *FRRS1L*, *RORB*, *PTPRZ1*, *DLGAP1*, and *TMEFF2* mRNAs by RT-qPCR. The expression level of each gene was measured in RNA isolated from three replicate samples from each of the three clonal HEK293 cell lines expressing either NOCTΔ(2–15)-3F or GST-3F. The $\log_2$ -fold change of each gene was then calculated as described under "Experimental procedures" and plotted along with the $\log_2$ -fold changes measured in the RNA-Seq analysis. The 95% credible intervals for each measurement are indicated *above* and *below* the mean $\log_2$ -fold change values. The *asterisk* indicates that the observed -fold change measured in the RNA-Seq assay has an FDR-corrected *p* value of $<1 \times 10^{-8}$. For the RT-qPCR measurements, the *black star* indicates that there is a >95% posterior probability of a change of 2-fold. The *B2M*, *ACTB*, and *TBP* mRNAs were also measured and were unchanged in both RNA-Seq and RT-qPCR assays. Data and statistics are reported in Table S2.

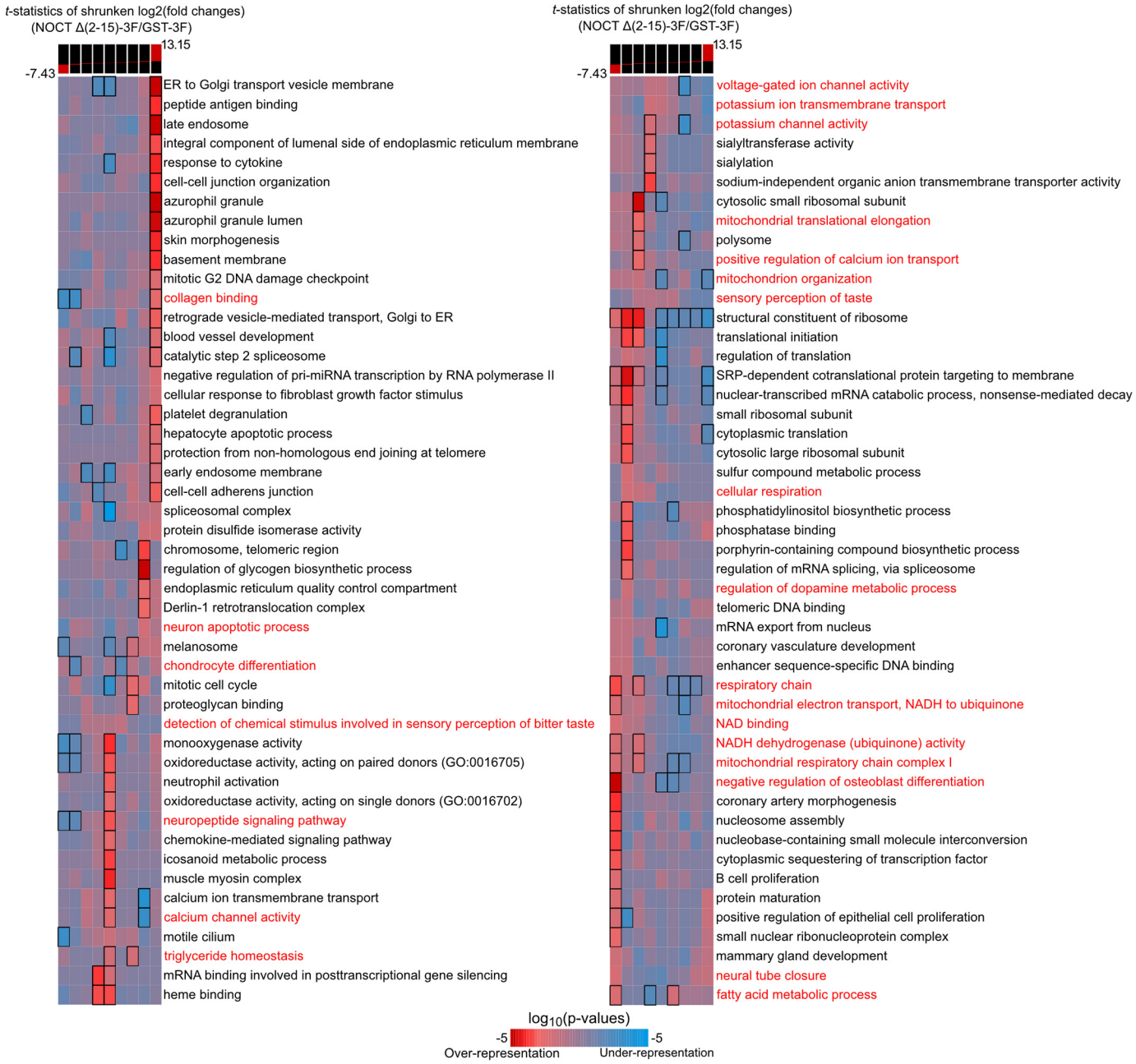

Figure 6. Pathway enrichment analysis of gene expression changes in response to NOCTΔ(2–15)-3F. iPAGE was applied to identify pathways with significant mutual information with the observed expression changes. Expression changes are quantified using the *t* statistic of gene-specific shrunken $\log_2$ -fold changes estimated by DESeq2 (see "Experimental procedures" for details). The *top panels above* each heat map show how iPAGE divided the DESeq2 gene set into nine groups with equal gene counts based on the measured expression changes; the *red range* in each bin indicates the range of *t* statistics encompassed by that bin. The *leftmost* bin contains genes with the most negative gene expression change metrics, and the *rightmost* bin contains the most positive. The *tile color intensities* were quantified by $\log_{10}$ of the GO term enrichment *p* values from iPAGE. The *colors* of *tiles* show $\log_{10}$ *p* values for significant over- (*red*) or underrepresentation (*blue*) of genes in the corresponding expression bin. Terms with names in *red type* are relevant to functional categories highlighted in the text and supporting information, including functions related to bone or lipid homeostasis, mitochondria, NAD metabolism, and neuronal functions (Figs. S5–S8, respectively, for each category). The in-plot descriptions for GO terms GO:0016702 and GO:0016705 are abbreviated and supplied with term numbers. *Heavy tile borders* indicate significant enrichments within a specific expression bin ($p < 0.05$ after Bonferroni correction across the rows of terms). Note that all displayed GO terms have significant mutual information with the overall gene expression change profile (as assessed by the default series of tests used by iPAGE; see "Experimental procedures" for details). Tables S1 and S3 describe the RNA-Seq data and statistics used in this analysis.

not appear to disrupt cellular bioenergetics, nucleotide biogenesis, or cell viability in the conditions tested.

Discussion

The results of this research provide important new insights into the molecular functions, expression pattern, and localization and processing of human NOCT, and its impact on metabolism of mRNAs and NAD cofactors. We found that NOCT protein is expressed and differentially processed in a cell type– and tissue–specific manner. The processing is consistent with mitochondrial targeting of NOCT. Indeed, we showed that NOCT can be localized into mitochondria, dependent on an N-

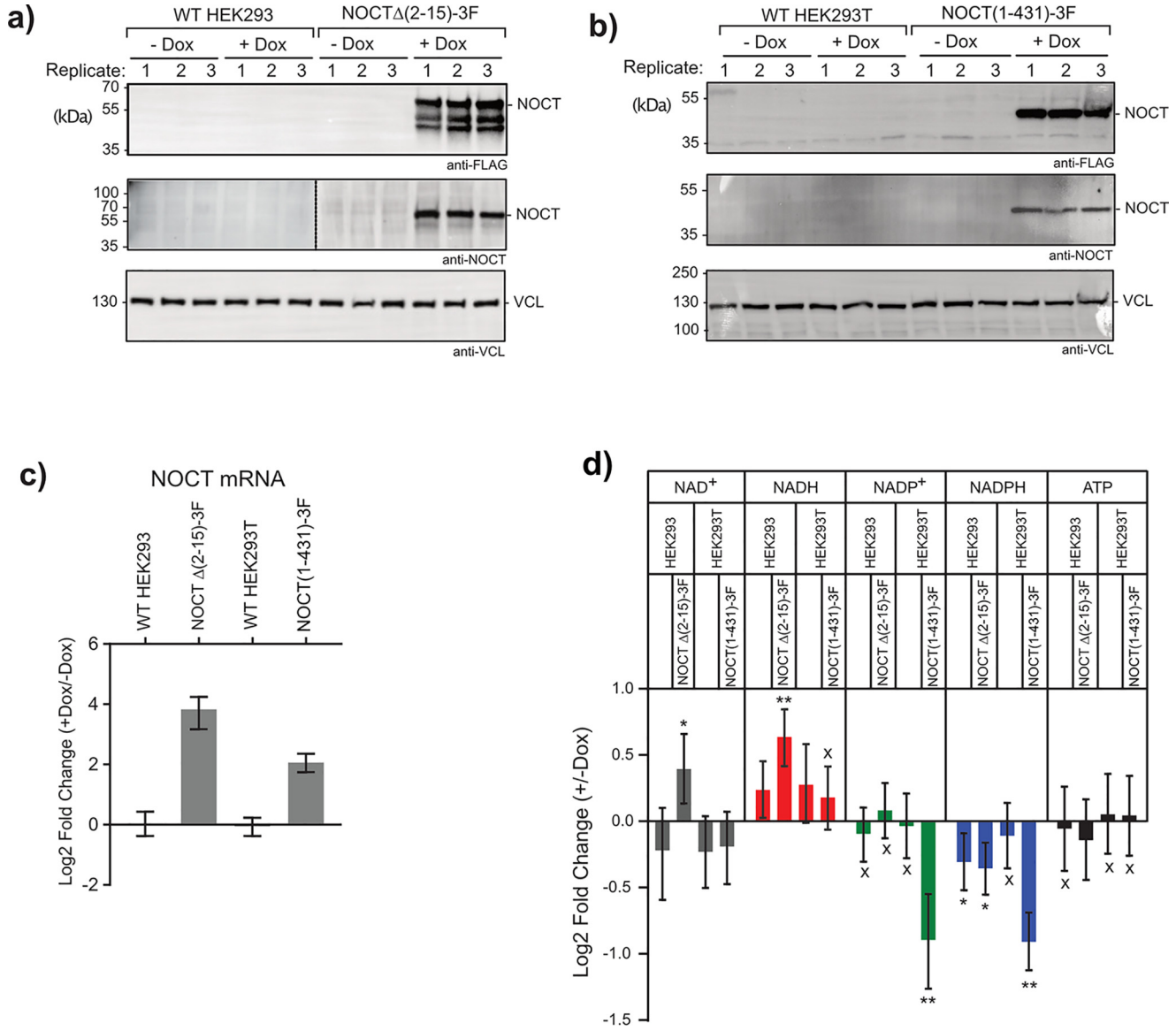

Figure 7. Effect of NOCT on cellular levels of NADH cofactors and ATP. *a*, Dox-inducible expression of NOCTΔ(2–15)-3F was confirmed in three separate pools of stably transduced HEK293 cells by performing anti-FLAG and guinea pig anti-NOCT Western blotting. NOCTΔ(2–15)-3F protein migrated with an apparent molecular weight of 58 kDa, consistent with unprocessed NOCT. WT HEK293 cells served as negative controls. Cells were treated with 1 μg/ml Dox (+*Dox*) for 72 h or the DMSO vehicle (−*Dox*). Equal mass of each cell lysate was loaded into each well, and VCL was detected by Western blotting to assess equivalent loading of lanes. The *vertical dashed line* indicates where the blot was cropped to assemble the figure. *b*, as in *a*, but using HEK293T cells with Dox-inducible NOCT(1–431)-3F that was introduced by the Flp-In T-REx system. NOCT(1–431)-3F protein migrated with a molecular mass of 44 kDa, consistent with mitochondrial protease processing. WT HEK293T cells served as negative controls. *c*, overexpressions of the stably expressed Dox-inducible NOCT constructs in the cell lines used in *a* and *b* were quantitated at the mRNA level using RT-qPCR. Each *bar* in the graph represents $n = 9$ from three replicate experiments with three biological replicates each. Log_2 -fold change values were calculated for NOCT mRNA in the presence of Dox relative to without Dox. Mean log_2 -fold change values are plotted along with 95% credible intervals. Data and statistics are reported in Table S2. *d*, NOCTΔ(2–15)-3F significantly increased levels of NAD^+ and NADH, whereas NOCT(1–431)-3F significantly decreased levels of $NADP^+$ and NADPH. The Dox-inducible and control cell lines were treated with either DMSO or 1 μg/ml Dox for 72 h. The levels of NAD^+, NADH, $NADP^+$, NADPH, and ATP were then measured in equal numbers of cells for each condition. Mean log_2 -fold change in each metabolite was calculated in the Dox-induced condition relative to the uninduced condition. Mean log_2 -fold change values are plotted for each measurement, along with 95% credible intervals. Measurements were derived from three replicate experiments, each of which contained three biological replicates. For significance calling, an *asterisk* denotes a posterior probability of >0.95 that the difference relative to the negative control is in the indicated direction. The *double asterisk* indicates a posterior probability of >0.95 that the indicated difference is at least 1.3-fold. An *x* marks a posterior probability of >0.95 that the indicated difference is no more than 1.3-fold in either direction. Data and statistical values are reported in Table S2.

terminal mitochondrial targeting sequence. In corroboration, two new studies also detected overexpressed NOCT in mitochondria (25, 26).

Our study reveals tissue-specific expression and processing of human NOCT. *NOCT* mRNA is most abundant in tissues such as adipose, breast, lung, liver, skeletal muscle, and kidney (Fig. S1), and NOCT protein is abundant in liver, kidney, skeletal muscle, and brain (Fig. 4). Interestingly, the kidney and liver exclusively express the unprocessed ~55-kDa form of NOCT (which, based on our analysis of HepG2 cells, likely would be in the cytosol and cytosolic surface of the mitochondria), whereas skeletal muscle expressed only the processed ~40-kDa form

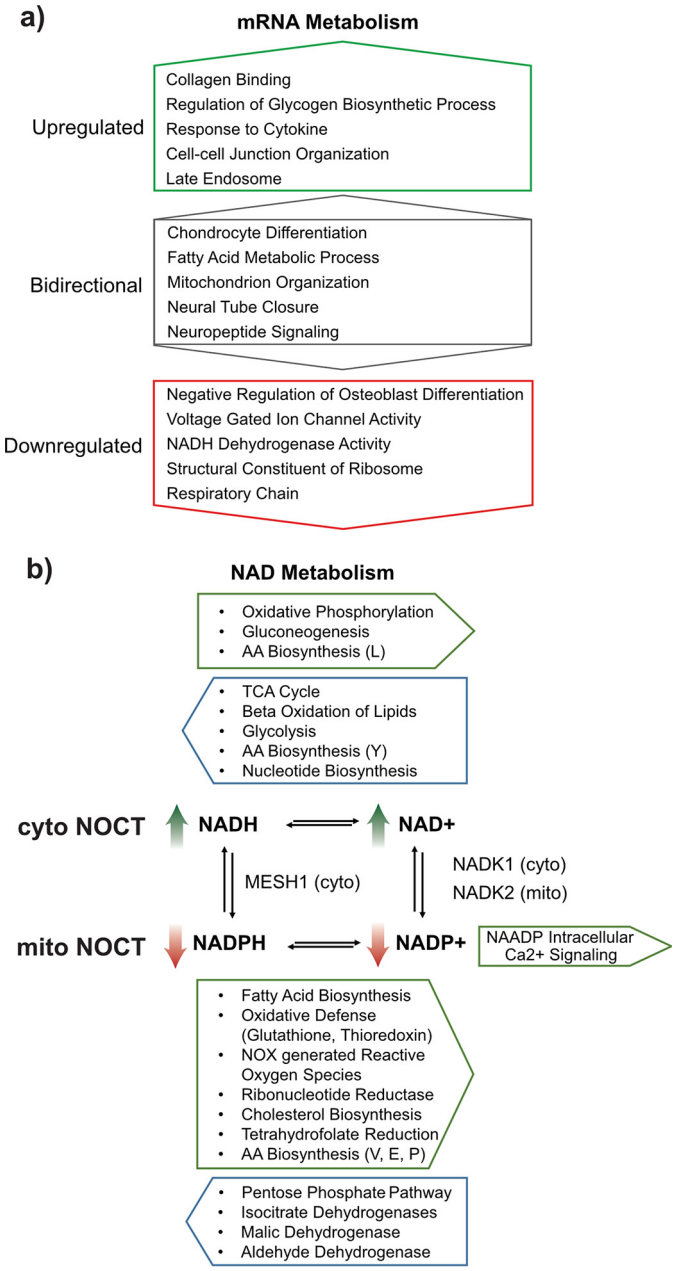

Figure 8. Summary of NOCT-mediated effects on mRNA and NAD metabolism. *a*, overexpressed, cytoplasmic NOCT altered the levels of mRNAs from genes that are enriched in multiple GO terms. Examples of significantly overrepresented GO terms among genes whose levels were either increased (up-regulated) or decreased (down-regulated) by cytoplasmic NOCT are shown. The bidirectional category provides examples of enriched GO terms containing different member genes that exhibited up- and down-regulation. *b*, diagram of NAD cofactor metabolism and the effect of overexpressed forms of NOCT. NAD cofactors are metabolized by a variety of anabolic (*green*) and catabolic (*blue*) pathways, indicated *above* and *below*, which interconvert NAD cofactors between redox states. $NADP^+$ can also be converted to the signaling molecule NAADP. In addition, NAD cofactors are interconverted between phosphorylation states, catalyzed by at least two kinases (NADK1 and NADK2) and phosphatases (MESH1 and NOCT). These kinases exhibit specific subcellular localization between cytoplasm (*cyto*) and mitochondria (*mito*), as indicated. *Green arrows* indicate the observed effect of cytoplasmic NOCT on increased NADH and NAD^+ levels. *Red arrows* indicate the observed effect of mitochondrial NOCT on decreased levels of NADPH and $NADP^+$.

and the brain produced both forms. These observations indicate that import and processing of NOCT are regulated by an unknown mechanism that should be the focus of future studies.

Whereas several other examples of differential cytoplasmic-mitochondrial localization have been reported, those cases involve utilization of distinct translation initiation sites to produce protein isoforms that either possess or lack an MTS (50–52). In contrast, our data indicate that NOCT translation initiates at Met-1 and that differential localization of NOCT is controlled through regulation of MTS-mediated import. In one reported case, both types of mechanisms appear to operate: differential usage of translation initiation sites can produce the CNP2 protein isoform that has an extended N-terminal containing an MTS, and subsequent phosphorylation of that MTS prevents mitochondrial localization (52). Although several phosphorylation sites have been mapped in NOCT, they were not within the MTS (53). Future research will be necessary to determine the precise mechanism that controls NOCT mitochondrial import and processing in different tissues.

Differential localization of NOCT to the cytoplasm or mitochondria has important implications for the repertoire of substrates it may act on. Cytoplasmic NOCT would be expected to affect nucleus-encoded mRNAs, which is consistent with the changes in mRNA abundance observed when NOCT expression is perturbed in our RNA-Seq data and previous studies (17–19). The vast majority of mitochondrial proteins are nucleus-encoded, some of which showed modest transcript level changes upon NOCT overexpression (Figs. S6 and S9). The human mitochondrial genome encodes just 13 mRNAs that produce a subset of oxidative phosphorylation proteins, two rRNAs, and 22 tRNAs (54). As expected, based on its cytoplasmic localization, overexpression of NOCTΔ(2–15) had minimal effects on levels of RNAs encoded by the mitochondrial genome (Fig. S9).

The impact of mitochondrial NOCT on mitochondrial genome–encoded RNAs remains to be fully explored. Regulation of these mitochondrial transcripts would likely alter metabolism and cellular energy states (55). In our analysis, we did not detect alteration of cellular bioenergetics (*i.e.* ATP levels) by either mitochondrial or cytoplasmic NOCT. Moreover, a recent report analyzed the effect of knockout of NOCT in mouse brown adipose and observed little to no effect on mitochondrial gene expression, although a subset of mitochondrially encoded mRNAs showed a modest decrease in expression during cold adaptation (20).

To gain insight into the genes and potential biological functions that NOCT may affect, we analyzed the impact of cytoplasmic NOCT on expression of nucleus-encoded transcripts and observed that hundreds of mRNAs were significantly affected. Multiple gene ontology terms were enriched in the down-regulated genes (Fig. 8*a*), notably negative regulation of osteoblast differentiation. Relevant to this category, NOCT was shown to negatively regulate osteoblastogenesis, and knockout of NOCT resulted in an increase in bone density (10, 41, 51). We identified *RORB* mRNA as a NOCT-repressed target. *RORB* is a regulator of osteoblastogenesis and affects bone density and resorption during aging (35), suggesting that *RORB* may be an important target of NOCT in bone development and maintenance.

We also identified multiple enriched GO terms that are related to mitochondrial components and functions and NAD

metabolism (Fig. 6 and Fig. S7). The magnitudes of NOCT effects on the individual genes in these categories are modest, but collectively they were statistically significant and may be germane to NOCT's association with the mitochondria and NAD metabolism (24).

Neuronal gene ontology categories were also significantly enriched in genes that are repressed by NOCT (Fig. 6 and Fig. S8), including voltage-gated ion channel activity. As described under "Results," transcripts from multiple neuron-specific genes were among those most substantially reduced by NOCT. This connection was likely facilitated by the neuron-like characteristics of HEK293 cells (35, 36). Further indication of a role of NOCT in neuronal gene regulation is the fact that unprocessed NOCT is expressed in human and mouse brains (Fig. 4). Currently, the potential neuronal functions of NOCT remain unexplored and should be investigated using brain-specific knockout models with analysis of neurological phenotypes.

The relationship between the effects of NOCT on transcript levels and the reported lipid metabolism phenotypes remains obscure. Knockout of *NOCT* in mice resulted in resistance to high-fat diet–induced obesity, coupled with reduced uptake, transport, and storage of fat (4, 8, 9). We observed that NOCT overexpression caused changes to potentially pertinent GO-term categories, such as triglyceride homeostasis and fatty acid metabolic process (Fig. 6 and Figs. S5 and S6), but in general with less uniform changes than those observed for the other terms noted above. For instance, NOCT had bidirectional effects on the different genes within certain GO terms (Fig. 8*a*). Interestingly, NOCT overexpression caused an apparent reciprocal switch in isoenzyme expression of 2,4-dienoyl-CoA reductases, DECR1 and DECR2 (Fig. S6*a*), which are involved in β-oxidation of polyunsaturated fatty acids. NOCT significantly reduced *DECR2* mRNA, a peroxisomal form of the isoenzyme, whereas the *DECR1* mRNA, encoding a mitochondrial form, increased. The potential physiological relevance of this observation will require future exploration.

Collectively, our RNA-Seq data, coupled with previous studies, provide evidence demonstrating a role of NOCT in mRNA metabolism, consistent with its proposed function as an exoribonuclease. The fact that NOCT affects a subset of transcripts indicates that a mechanism conferring transcript specificity exists but remains unknown. Other RNA-degrading enzymes can be directed to their target RNAs through sequence-specific recognition of cis-acting RNA elements, often conferred through partnership with RNA-binding proteins (7). We were unable to identify enrichment of cis-regulatory elements in the NOCT-regulated transcripts in our data set. Future studies are necessary to determine how NOCT regulates these RNAs and to identify putative protein partners that may regulate its activity and specificity.

Our results build upon a recent report that NOCT can dephosphorylate $NADP^+$ and NADPH *in vitro* (25). We find that overexpression of cytoplasmic NOCT increased the cellular pool of NADH and NAD^+ levels, whereas mitochondrial NOCT decreased the level of $NADP^+$ and NADPH (Fig. 8*b*). Overall, these observations are consistent with the NADP(H) phosphatase activity of NOCT. The implications are intriguing but complex. NAD cofactors exhibit high flux between redox states through crucial roles in biosynthetic and catabolic pathways, cellular bioenergetics, protection from and generation of reactive oxygen species, and signal transduction (summarized in Fig. 8*b*) (56–58). NAD cofactors also interchange between cytoplasmic and mitochondrial compartments (57, 59–62). Germane to NOCT, NAD is also interconverted between phosphorylation states by specific cytoplasmic and mitochondrial kinases, NADK1 and NADK2, respectively (Fig. 8*b*) (63, 64). Additionally, another cytoplasmic NADPH phosphatase, MESH1/HDDC3, has now been described (65) and is expressed more broadly than NOCT (Fig. S4). We considered the possibility that NOCT might alter expression of these NAD-interconverting enzymes; the abundant expression of NADK1, NADK2, and MESH1 mRNAs was not affected by overexpressed cytoplasmic NOCT (Table S1). Our data, coupled with the data of Estrella *et al.* (24), indicate that the NADP(H) phosphatase activity of NOCT contributes to NAD cofactor interconversions. The differential localization of NOCT to cytoplasm or mitochondria suggests that it may alter NAD-linked metabolism in a cell type– and tissue type–specific manner.

A broad implication of the NADP(H) phosphatase activity of NOCT is that it could alter cellular metabolism. Dephosphorylation of NADP(H) would increase cellular NAD(H) pools and generally promote catabolic pathways, including glycolysis, β-oxidation of fatty acids, and oxidative phosphorylation (Fig. 8*b*). Such changes would be anticipated to promote ATP production, although we did not detect such an effect. It is also worth considering how NOCT NADP(H) phosphatase activity may relate to the reported lipid metabolism and storage defects observed in the knockout mice. Loss of NOCT activity should increase the pool of NADP(H) and thereby promote biosynthetic pathways, including synthesis of lipids (Fig. 8*b*). This prediction is seemingly at odds with the observed loss of adipose tissue and defects in lipid update, transport, and storage observed in the *NOCT* knockout mice (4, 8). Clearly, more research is necessary to determine whether the NADP(H) phosphatase activity of NOCT is relevant to the reported resistance to fat-induced obesity phenotype or whether the exoribonuclease function of NOCT is more important for this phenotype.

The emerging picture indicates that NOCT may be a dual-function enzyme that controls RNA and NADP(H) metabolism. Thus, it joins the growing ranks of "moonlighting" metabolic enzymes that fit the REM (RNA-enzyme-metabolite) hypothesis (66–70). Recent global surveys have identified more examples of moonlighting RNA-binding proteins, suggesting that many of these dual-function enzymes provide a level of translational control in response to metabolic states (70). Interestingly, six NAD cofactor–utilizing enzymes have been found to also bind to mRNAs. One example is glyceraldehyde-3-phosphate dehydrogenase (GAPDH), which binds to AU-rich RNA elements of specific mRNA transcripts within the same binding site that binds NAD^+ (71–73). Future work on NOCT will be crucial for determining the contributions of the NOCT NADP(H) phosphatase and mRNA repression activities and differential localization to the control of gene expression and metabolism.

Experimental procedures

Plasmids

The pFC3F plasmid backbone was generated from the pF5A vector (Promega) to generate C-terminal 3×FLAG tag fusions. Human NOCT(1–431) or *Schistosoma japonicum* GST coding sequences were inserted into pFC3F using the Flexi Cloning System (Promega). To generate NOCTΔ(2–15)-3F, residues 2–15 were removed using inverse PCR. NOCT N-terminal point mutants were generated from pCR4 TOPO NOCT (Open Biosystems) and QuikChange site-directed mutagenesis PCR (Agilent) to generate NOCT(1–431) M1X and NOCT(1–431) M67G. NOCTΔ(2–15) and NOCTΔ(2–15) M67G were generated from pCR4 vectors using inverse PCR. All NOCT inserts generated in pCR4 TOPO were then transferred to pF5A by Flexi Cloning. To generate NOCT(1–86) EGFP, the EGFP ORF was PCR-amplified from the pEGFPN1 vector (Clontech) with appended 5′ AfeI and 3′ EcoRI restriction sites. pF5A NOCT (1–431) was digested with AfeI and EcoRI to remove NOCT (87–431), which was replaced by the EGFP ORF. The initiator methionine codon of the EGFP ORF was not included in this construct. NOCTΔ(2–15)-3F pCW57.1 was generated using the pCW57.1 (Addgene accession no. 41393) plasmid backbone. NOCTΔ(2–15)-3F was PCR-amplified and inserted into pCW57.1 using Gibson Assembly with NEBuilder HiFi Assembly Master Mix (New England Biolabs). NOCT(1–431)-3F pcDNA5/FRT/TO was generated through PCR amplification of NOCT(1–431) cDNA (Source Biosciences I.M.A.G.E. clone 8322546) with appended 5′ BamHI and 3′ NotI restriction sites. The NOCT PCR insert and pcDNA5/FRT/TO were digested with BamHI and NotI restriction enzymes (New England Biolabs) followed by ligation. All constructs were confirmed by DNA sequencing.

Generation of α-NOCT antibodies

The rabbit α-NOCT polyclonal antibody was produced in rabbits inoculated with MBP-NOCT(1–431) (Thermo Fisher Scientific custom antibody services). This MBP-NOCT antigen (residues 1–431) was expressed in BL21 DE3 cells and purified over amylose resin. Crude serum was tested for reactivity against HEK293 cell extracts overexpressing HaloTag-NOCT (1–431). NOCT antibodies were then purified from the verified serum by ammonium sulfate fractionation and then antigen affinity purification using recombinantly expressed HaloTag-NOCT(1–431) immobilized on HaloLink resin (Promega). The serum was purified over the immobilized NOCT column before elution with 5 M NaI and 1 mM ammonium thiocyanate. Antibody was subsequently dialyzed into 1× PBS (137 mM NaCl, 27 mM KCl, 10 mM Na_2HPO_4, and 18 mM KH_2PO_4) for 1 h at 4 °C. Dialysis was repeated two additional times with the final dialysis step performed overnight. Insoluble material was removed by centrifugation at 18,000 × *g*, and the antibody was concentrated to 1 mg/ml using a Centricon spin concentrator (Millipore Sigma). Purified polyclonal antibody was verified for reactivity against recombinant purified rNOCT(64–431) (purified as described by Abshire *et al.* (1)), as shown in Fig. 1.

The guinea pig α-NOCT polyclonal antibody, used in Figs. 2 and 7, was produced in guinea pigs inoculated with Strep(II)-Sumo-NOCT(64–431) (Cocalico custom antibody services). Briefly, Strep(II)-Sumo-NOCT(64–431) was recombinantly expressed in BL21 DE3 Rosetta2 STAR cells and purified over Strep-Tactin Superflow Plus resin (Qiagen). Crude serum was verified for reactivity against recombinant NOCT (64–431) and HEK293 cell extracts from HEK293 cells stably overexpressing NOCT(1–431)-3F. Antibody from verified serum was purified using Protein A-agarose (Pierce), and the antibody fraction was eluted using 0.1 M glycine and 20% glycerol. Eluates were neutralized with 0.15 M Tris, pH 8, and the α-NOCT antibody was then antigen affinity–purified with NOCT(64–431) immobilized on Immobilon-P PVDF membrane (Millipore). Guinea pig α-NOCT was eluted from the membrane with 0.1 M glycine and 20% glycerol. Eluates were neutralized with 0.15 M Tris, pH 8, before the antibody was concentrated to ∼0.1 mg/ml using a Centricon spin concentrator. Purified polyclonal antibody was verified for reactivity against recombinant purified NOCT(64–431) and lysates from HEK293 cells stably overexpressing NOCT(1–431)-3F.

Analysis of differential NOCT processing by Western blotting

HEK293 cells were cultured in DMEM (Fisher), 1% penicillin/streptomycin/glutamine (Fisher) and 10% FBS (Thermo) at 37 °C and 5% CO_2. Cells were transfected with NOCT N-terminal mutant constructs using Fugene HD (Promega) in a ratio of 3 μl of transfection reagent per 1 μg of DNA. HCT116 cells were cultured as described for HEK293 cells but in McCoy's 5A medium (Fisher), 1% penicillin/streptomycin/glutamine, and 10% FBS. Cells were transfected using Fugene HD (Promega) in a ratio of 4 μl of transfection reagent per 1 μg of DNA. Both HEK293 and HCT116 cells were harvested and resuspended in modified radioimmunoprecipitation assay (mRIPA) buffer (10 mM Tris (pH 8.0), 140 mM NaCl, 1 mM EDTA, 0.5 mM EGTA, 1% (v/v) Triton X-100, 0.1% (w/v) sodium deoxycholate, and 0.1% (w/v) SDS) for lysis containing complete protease inhibitor mixture (Roche Applied Science). Lysates were homogenized using a handheld cell disruptor, and sample concentrations were determined using a DC Lowry protein assay (Bio-Rad). For cell lysates, equal masses of protein samples (20 μg) were resolved using SDS-PAGE and then transferred to Immobilon-P PVDF membrane (Millipore). Purified rNOCT(64–431) (6 ng) was used as a positive control for NOCT and was expressed and purified as described previously (1). Blots were probed using the following primary antibodies: α-NOCT (derived from rabbit serum, detecting NOCT MTS mutants expressed from pF5A), α-EGFP (detecting EGFP and NOCT (1–86)-EGFP, Clontech clone JL-8), and α-FLAG (detecting C-terminal 3×FLAG-tagged constructs, Sigma). Blots were probed using HRP-conjugated secondary antibody (Sigma) and Immobilon Western HRP chemiluminescent substrate (Millipore) before imaging on a ChemiDoc Touch (Bio-Rad). As loading control, either vinculin (VCL) or GAPDH was detected on the same blots using α-vinculin antibody (Thermo Fisher) or α-GAPDH antibody (Ambion).

Analysis of human and mouse tissue blots

Pretransferred blots of tissue extract panels from human and mouse were purchased from Novus Biologicals (Insta-blot NBP2-31378 and NBP2-20111). According to the manufacturer, each blot contains 50 μg of total protein from the indicated tissue type. Tissues were from donors with no known disease, and proteins were extracted using lysis buffer (10 mM Tris, pH 8.0, 130 mM NaCl, 1% Triton X-100, 10 mM NaF, 10 mM NaP_i, 10 mM $NaPP_i$) with protease inhibitor mixture. Blots were hydrated, stained with amido black, imaged, and then blocked before probing with the α-NOCT antibody derived from rabbit serum. Blots were probed using HRP-conjugated goat α-rabbit IgG secondary antibody (Sigma) and Pierce ECL Western blotting substrate before imaging on a Chemidoc Touch (Bio-Rad).

Generation of cell lines

All parental cell lines were purchased from the American Type Culture Collection, unless otherwise noted. To produce stably transfected HEK293 cell lines (ATCC), cells were transfected with a 1:10 molar ratio of pEF6 HisA (Invitrogen) to either GST-3F pFC3F or NOCTΔ(2–15)-3F pFC3F using Fugene HD. 5 μg/ml Blasticidin S (Thermo Fisher Scientific) was used to select blasticidin-resistant populations that were then subcloned using the dilution method. Blasticidin-resistant clones expressing 3×FLAG-tagged fusion proteins for each construct were identified by Western blotting using α-FLAG. Briefly, cells were harvested in 1× PBS, pelleted, and frozen. Prior to use, cell pellets were resuspended in mRIPA supplemented with protease inhibitor (Millipore Sigma) for lysis. Lysates were homogenized using a handheld cell disruptor, and sample concentrations were determined using the Bio-Rad DC Lowry assay. Each sample (10 μg of total protein) was resolved on 4–20% TGX gradient gels (Bio-Rad) and then transferred onto Immobilon-P PVDF membrane. Blots were probed using α-FLAG (Sigma) before detection using HRP-conjugated secondary antibody (Sigma) and ECL Western blotting substrate (Pierce) before imaging on a ChemiDoc Touch (Bio-Rad).

To generate HEK293 cells expressing NOCTΔ(2–15)-3F under the control of the tetracycline operator, lentivirus was produced in HEK293FT cells transfected with NOCTΔ(2–15)-3F pCW57.1 and the pRSV-Rev (Addgene accession no. 12253), pMD2.G (Addgene accession no. 12259), and pMDLg/pRRE (Addgene accession no. 12251) packaging vectors. HEK293 cells were transduced with 400 μl of viral supernatant and 6 μg/ml Polybrene in a 1-ml final culturing volume per well in a 6-well plate. The population of treated HEK293 cells was selected for cells with genomic integration with 1 μg/ml puromycin. A population of puromycin-resistant cells was treated with 1 μg/ml doxycycline (Sigma) for 48 h. To verify expression of NOCTΔ(2–15)-3F, the transduced and selected populations of HEK293 cells were harvested, pelleted, and lysed as described above. Expression of NOCTΔ(2–15)-3F was verified by Western blotting with α-FLAG (Sigma).

To produce tetracycline-inducible, Flp-In NOCT(1–431)-3F HEK293T cell lines, parental Flp-In HEK293T cells (Invitrogen) were transfected with NOCT(1–431)-3F pcDNA5/FRT/TO and pOG44 using Lipofectamine 3000 (Invitrogen) according to the manufacturer's instructions. Cells with genomic integration were selected for using 100 μg/ml hygromycin (Gibco) and 10 μg/ml blasticidin (Gibco). Single colonies were generated from the antibiotic-resistant population and verified using α-FLAG Western blotting.

Immunofluorescence

Human 143B, HEK293, and HepG2 cell lines were cultured for use in immunocytochemistry experiments in DMEM supplemented with 10% (v/v) FBS, 2 mM GlutaMax (Gibco), and 1× penicillin/streptomycin at 37 °C under 5% CO_2. For each construct, 1.5–2 μg of plasmid was transfected into cells at 40% confluence using Lipofectamine 3000 transfection reagent (Thermo Fisher Scientific) according to the manufacturer's instructions. After 24 h, cells were split onto microscope slides, and at 48 h post-transfection, cells were incubated for 35 min with 200 nM MitoTracker Red CMXRos (Thermo Fisher Scientific) at 37 °C. Cells were washed one time with prewarmed DMEM and once with Dulbecco's PBS before fixing in PBS + 4% formaldehyde for 15 min at room temperature. Cell permeabilization was performed by incubating cells in PBS + 5% FBS (PBSS) supplemented with 1% Triton X-100 for 5 min at room temperature. Cells were washed twice with 1× PBSS (without Triton X-100) and blocked with PBSS for 1 h. To visualize 3×FLAG-tagged proteins, cells were incubated with 1:200 mouse anti-FLAG M2 antibody (Sigma–Aldrich, F3165) for 2 h at room temperature, followed by triplicate 5-min washes with PBSS. Cells were then incubated with 1:1000 goat anti-mouse Alexa Fluor Plus 488 (Thermo Fisher Scientific, A32723) for 1 h at room temperature before slides were washed three times with PBSS for 5 min each. DAPI staining (300 nM; Sigma–Aldrich) was performed during the first of the final washes. Immunofluorescence images were captured using a Zeiss LSM800 confocal microscope, and Fiji software was used to produce the merged images.

Subcellular fractionation of cells

For subcellular fractionation of HepG2 cells or HEK293T cells that express NOCT(1–431)-3F, mitochondrial isolation was performed as described previously, with the omission of the sucrose gradient step (74). Mitochondrial pellets were gently resuspended in MSH buffer (210 mM mannitol, 175 mM sucrose, 20 mM DTT, 0.2 mM phenylmethylsulfonyl fluoride, and 1× protease inhibitor mixture (Roche Applied Science)). The protein concentration of the total cellular, cytoplasmic, and mitochondrial fractions was measured using the DC Lowry protein assay (Bio-Rad). Mitochondrial fractions were subjected to no treatment, treatment with proteinase K (20 μg/4 mg of mitochondrial protein; Thermo Fisher Scientific), or treatment with proteinase K + 1% Triton X-100 to expose intramitochondrial proteins to protease activity. Equal volumes of treated mitochondrial fractions and cytoplasmic and nuclear fractions with protein concentrations equal to the untreated mitochondrial fraction were resolved via SDS-PAGE followed by Western blotting as described above.

Immunoblotting was performed using the following antibodies: goat anti-DDDDK (FLAG) (1:5000; Abcam, ab1257), guinea pig anti-NOCT (described above), rabbit anti-uL4m antibody (1:2000; Sigma, HPA051261), rabbit anti-uS15m antibody (1:2000; ProteinTech Group, 17006-1-AP), mouse anti-mitofusin (1:1000; Abcam, ab56889), rabbit anti-TOM20 (1:2000; Cell Signaling Technology, 42406), rabbit anti-histone H3 (1:1500; Abcam), mouse anti-uL1 (1:1000; Santa Cruz Biotechnology, Inc., sc-100827). Secondary antibodies used were mouse anti-goat IgG–HRP (1:5000; Santa Cruz Biotechnology, Inc., sc-2354), ECL sheep anti-mouse IgG-HRP (1:3000; GE Healthcare, NA9310V), and ECL donkey anti-rabbit IgG-HRP (1:3000; GE Healthcare, NA9340V). Immunoblots were developed using Clarity Western ECL substrate (Bio-Rad).

RNA-Seq sample preparation

For each clonal cell line (three lines expressing GST-3F and three lines expressing NOCTΔ(2–15)-3F), two 10-cm dishes were plated with 3×10^6 cells in DMEM + 10% FBS and incubated for 3 days at 37 °C and 5% CO_2. Cells were harvested by dissociation with TrypLE (Thermo), washed twice with cold 1× PBS, pH 7.4 (Gibco), and rapidly frozen at −80 °C. Expression of GST-3F and NOCTΔ(2–15)-3F was verified by Western blotting using α-FLAG as described above. Total RNA was isolated from frozen cell pellets using a Maxwell RSC SimplyRNA Cells kit (Promega) using a 2× concentration of DNase I. RNA was eluted in 50 μl of nuclease-free water and was analyzed using a Bioanalyzer Tapestation (Agilent), with RIN (RNA integrity number) values between 9.6 and 10.0. Total RNA (5 μg) was combined with ERCC spike-in standards (5 μl of 1:50 diluted stock solution; Invitrogen) and submitted to the University of Minnesota Genomics Center for library generation and sequencing. RNA TruSeq strand-specific 50-bp dual-indexed RNA libraries were prepared using RiboZero rRNA depletion (Illumina) and sequenced on a HiSeq 2500 in high-output mode. Library generation and sequencing was performed by the University of Minnesota Genomics Center.

RNA-Seq data analysis

Raw RNA-Seq data for each sample contained between 34,593,128 and 40,679,504 paired-end reads, with both read 1 and 2 of length 51 bases. We used FastQC (75) with MultiQC (76) to examine the quality of the sequencing reads. The average quality per position of the sequencing reads for each sample sequencing read file ranged from 29.65 to 37.38. For both read 1 and read 2 of each sample, bases at positions 1–10 showed a noticeable nonrandom overrepresentation of specific bases, likely coming from adaptor sequences. We trimmed the first 10 bases for both read 1 and read 2 for all samples using Cutadapt (version 1.8.1) to remove a fixed number of bases from the 5′ end of reads 1 and 2 separately in single-end mode (-u 10) (77). We next performed a quality trimming using Trimmomatic (version 0.33) in paired-end mode requiring a minimum quality score for leading and trailing sequences of 3, a minimum average quality score of 15 within a window of 4 bases, and a minimum read length of 26 (LEADING:3 TRAILING:3 SLIDINGWINDOW:4:15 MINLEN:26). The minimum read length requirement is derived from STAR alignment recommendations (78, 79). Trimming survival rates of paired-end reads for all samples were >99%. Raw and processed data have been deposited to NCBI GEO (GSE142749). Code used for RNA-Seq data analysis is available at https://github.com/freddolino-lab/2019_nocturnin.

Alignments

For mapping of the sequencing reads, we built a reference for STAR (version 2.5.2b) that contains the human reference genome GRCh38 (release 92, accessed June 18, 2018), NOCTΔ (2–15)-3F pFC3F plasmid sequence, GST-3F pFC3F plasmid sequence, and the ERCC spike-ins. The STAR index was built from the customized combined genome with the above sequences as a FASTA file, annotations as a GTF file, and an overhang length of 100. For all samples, >91% of reads mapped uniquely as reported by STAR (80).

Quantification

We quantified the features from alignment results using HTSeq (version 0.6.1p1), with stranded set to reverse and requirement of minimum alignment quality score set to 10, supplied with customized annotations as used in alignment (81). The overlap resolution of feature quantification in HTSeq was set as −mode = union with −nonunique = none (*i.e.* counting overlaps of a feature with any position of a read toward the set of identified feature(s) of the corresponding read and ignoring ambiguous alignments to features). For all samples, the percentages of uniquely aligned read pairs assigned to nonambiguous features range from 61.74 to 66.35%, covering 26,221–27,756 of the 58,489 features in the input annotation.

Differential expression analysis

We performed differential expression analysis using DESeq2 (version 1.16.1) on the gene features quantified by HTSeq as described above (82). The three samples with NOCTΔ(2–15)-3F overexpression were treated as biological replicates in the NOCT group, and the three samples with GST-3F overexpression were treated as biological replicates for the GST group, with the GST group being the reference level in the subsequent differential expression analysis. Quantified gene features were prefiltered by requiring a total of counts from all samples to be greater than 10, leaving us with 23,417 features. We used the single-step wrapper function "DESeq" for standard differential expression analysis and then used a patched version function "lfcShrink" to show the estimated S.D. values of shrunken $\log_2$ -fold changes as additions to the results. The 95% confidence intervals of RNA-Seq expression changes as shown in Fig. 5*d* were calculated as shrunken $\log_2$ -fold change plus or minus 1.96 times the estimated S.D. in $\log_2$ -fold changes.

A total of 23,414 genes survived that had no count outliers (characterized by a non-NA p value from DESeq2), and 17,058 genes passed the independent filtering based on the mean of normalized counts in all samples for each feature (characterized by a non-NA p value when interpreting DESeq2 results) (83). Significance was determined by an FDR-corrected p value threshold of 0.05 with $\log_2$ -fold change cutoffs as specified for

a subset of analyses in the text. Statistics for all gene features passing the prefiltering are reported in Table S1. Gene expression changes in Fig. 5 are quantified as the shrunken $\log_2$ -fold change estimates of the NOCT group relative to the GST group. In the MA plot (Fig. 5*B*), the average expression levels were quantified as the mean of $\log_2$ transcripts per million (TPM) of six samples, including three replicates each in the NOCT and GST groups, and expression changes were quantified as shrunken $\log_2$ -fold changes. To calculate TPM, we used the median fragment length for each sample and the number of genomic positions that appear in at least one exon of an annotated transcript as the length of each gene. The volcano plot and the MA plot were generated with R (version 3.6.1), with major contributing packages including ggplot2 (version 3.1.1) and biomaRt (version 2.42.0).

The genes are divided into four categories based on the chromosome information from Ensembl (accessed via biomaRt) and Human MitoCarta2.0 (accessed November 11, 2019 with file first time stamped at July 21, 2015) (84, 85). We categorized genes annotated with chromosome MT as "mitochondrially encoded genes." For other genes, based on Human MitoCarta2.0, genes with "high confidence of mitochondrial localization (based on integrated proteomics, computation, and microscopy)" were categorized as "nucleus-encoded; with evidence for mitochondrial localization," and genes with ranked mitochondrial localization predictions using the training sets, proteomics data, and auxiliary data (86), were categorized as "nucleus-encoded; with no evidence for mitochondrial localization." Genes that are not listed in MitoCarta2.0 are listed as "unknown." The category for each gene is also reported in Table S1.

Pathway enrichment analysis

We used iPAGE to identify potential NOCT-regulated pathways as the informative GO terms in the NOCT sample group compared with the control GST group (46, 87, 88). First, a custom iPAGE database was built by retrieving gene and GO term information from Ensembl using the R package biomaRt (accessed August 27, 2018) (86, 89, 90). The custom database did not contain information of the overexpression components or ERCC spike-ins. We used the *t* statistics of shrunken $\log_2$ -fold changes as input for iPAGE, calculated as the shrunken $\log_2$ -fold changes divided by corresponding estimated S.D. values for all gene features for increased robustness. We set up iPAGE with nine equally sized bins for expression changes and disabled the default requirement of independence among detected GO terms. In Figs. S5–S8, we highlight a total of 24 GO terms of interest in four categories among the 96 iPAGE-detected GO terms discussed in the main text and show the shrunken $\log_2$ -fold changes of all genes that are associated with a specific GO term. Table S3 reports the list of iPAGE-identified GO terms (Fig. 6) and corresponding summary statistics for gene expression changes.

Reverse transcription and quantitative PCR

The MIQE reporting information for RT-qPCR assays is included in a supporting information file, along with sequences and details of primers. Three replicate samples of each of the clonal cell lines, which overexpressed either NOCTΔ(2–15)-3F or GST-3F produced for RNA-Seq, were grown in T75 flasks at 37 °C and 5% CO_2. Cells were trypsinized with TrypLE (Thermo) and resuspended in 10 ml of DMEM + 10% FBS (Thermo). Cells were collected by centrifugation at 1000 × *g* and stored at −80 °C as pellets until further use. The doxycycline-inducible cell lines (HEK293 TetON NOCTΔ(2–15)-3F and HEK293T Flp-In T-REx NOCT(1–431)-3F) and control parent lines (WT HEK293 cells (ATCC) and WT HEK293T Flp-In T-REx cells (Thermo)) were seeded and treated with either DMSO (−Dox) or 1 μg/ml doxycycline in DMSO (+Dox; Sigma) for 72 h. Cells were collected and stored as described above. RNA was harvested from each cell line using the Maxwell RSC SimplyRNA Cells Kit (Promega). Briefly, cell pellets were resuspended in 200 μl of Maxwell lysis buffer and then mixed with 200 μl of homogenization buffer with 1-thioglycerol. Lysates were added to the Maxwell RSC SimplyRNA Cells Kit cartridges along with a 2× concentration of Maxwell DNase I solution per cartridge. The Maxwell RSC SimplyRNA Cells protocol was run without modification on a Maxwell RSC instrument (Promega), and RNA was eluted in 40 μl of RNase-free water and stored at −80 °C.

RNA was quantified using absorbance at 260 nm on a Nanodrop One UV spectrophotometer (Thermo Fisher Scientific). Reverse transcription reactions were carried out using 500 ng of total RNA from each sample and the GoScript Reverse Transcription Mix, Random Primers Kit (Promega, A2800) according to the manufacturer's protocol. For each sample, control reactions without reverse transcriptase (RT) were generated to assess background from other sources of DNA. RT+ and RT− reverse transcription reactions were diluted 67-fold in RNase/DNase-free water, and RT-qPCR was performed on the CFX96 real-time system (Bio-Rad) using GoTaq qPCR master mix (Promega). Cycling parameters were as follows: 1) 95 °C for 2 min, 2) 95 °C for 15 s, 3) variable annealing temperatures for 1 min, and 4) 72 °C for 1 min. Steps 2–4 were repeated for a total of 40 cycles. Control reactions without template and without RT were performed for all primer sets. For each transcript, PrimeTime Assays (IDT) were used in qPCR experiments. For the cell lines generated for RNA-Seq, RT-qPCR was performed with all of the listed primers. For the doxycycline-inducible cell lines, qPCR was performed for NOCT and TBP transcript levels. Annealing temperatures for each primer set were optimized to 90–110% efficiency at 200 nM primer concentration. Cycle threshold (*Ct*) values were measured using the CFX Manager software.

To provide a consistent analysis of the RT-qPCR data, we applied a Bayesian hierarchical model using the STAN programming language via the brms R package (91–93). Our approach closely follows that used in Arvola *et al.* (94); we used as initial observables the efficiency-weighted *Cq* values of the NOCT and reference (TBP) transcripts within each experimental replicate (calculated as in Equation 3 of Refs. 94 and 95). We then fitted a linear model with Student's *t* distributed errors in which we considered each *Cq* value to arise due to a linear combination of terms from the target of interest (NOCT or TBP), target:genotype interaction,

target:genotype:induction interaction, target:date interaction (with date corresponding to the batch of which the sample was a part), and a group-level (random) effect for each biological replicate. *Cq* values were centered on zero prior to model fitting. We used a normal(0,3) prior for all population-level (fixed) effects and brms default priors for all other parts of the model. The model was fitted using six Monte Carlo chain runs for 5000 iterations each, and convergence was assessed using standard brms/STAN convergence checks and manual inspection of the posterior predictive distributions. Data and statistics values are reported in Table S2.

Cellular ATP assays

The following cell lines were used in these measurements: WT HEK293 (ATCC), HEK293 TetON NOCTΔ(2–15)-3F, WT HEK293T Flp-In T-REx cells (Thermo), and HEK293T Flp-In T-REx NOCT(1–431)-3F. HEK293 cell lines were plated in 6-well plates with 300,000 cells/well, and the HEK293T Flp-IN lines were plated at 500,000 cells/well in DMEM + 10% Tet-free FBS (Sigma) and 1× GlutaMAX (Sigma). One full 6-well tissue culture plate was seeded for each cell line used. Cells were cultured for 24 h before the induction of overexpression. For each cell line, 3 wells were treated with 1 μg/ml doxycycline (Dox+, Sigma) in DMSO or with DMSO (Dox−). Cells were incubated for 72 h postinduction before harvesting. Each well of HEK293 cells were harvested by treatment with 200 μl of TrypLE (Invitrogen). Detached cells were resuspended with 800 μl of DMEM + 10% FBS and cells. HEK293T cells were resuspended in 3 ml of culturing medium by pipetting. HEK293T cell suspensions were centrifuged at 1000 × *g* for 10 min to collect cells, and pellets were resuspended in 1 ml of DMEM + 10% FBS. Cells were counted by mixing a sample of the cell suspension with 0.4% trypan blue (Invitrogen) in a 1:1 ratio before counting on the Countess II cell counter (Invitrogen). For each sample, 20,000 viable cells were added to a 96-well white flat-bottomed plate (Nunclon). Each well was brought up to 100 μl of total volume with DMEM + 10% FBS. Three wells of DMEM + 10% FBS alone were added for blank measurements. 100 μl of reconstituted Cell Titer Glo reagent (Promega) was added to each well, and the plate was incubated for 10 min at room temperature before luminescence was measured using a GloMAX Discover Plate reader luminometer (Promega). Three replicate experiments were performed with three biological replicates for each cell type and treatment within each experiment for nine total measurements per cell type and treatment.

The cellular ATP assays were analyzed using Bayesian hierarchical models, following the same general approach as that outlined above for the analysis of RT-qPCR experiments. In this case, we took as primary data the 0-centered $\log_2$ luminescence measurements output by the GloMAX assay and fitted a model with population-level effects for the cell line, condition (induced *versus* uninduced), and condition:cell line interaction and group-level effects for the assay date, biological replicate, and date-treatment-cell line combination. We assumed Student's *t* distributed errors, with a normal(0,5) prior on the population-level effects and brms default priors for all other parameters. The model was fitted and assessed as described above for the RT-qPCR data. Data and statistics values are reported in Table S2.

Cellular metabolite assays

The following cell lines were used in these measurements: WT HEK293 (ATCC), HEK293 TetON NOCTΔ(2–15)-3F, WT HEK293T Flp-In T-REx cells (Thermo) and HEK293T Flp-In T-REx NOCT(1–431)-3F. HEK293 cell lines were plated in 6-well plates with 300,000 cells/well, and the HEK293T Flp-IN lines were plated at 500,000 cells/well in DMEM + 10% Tet-free FBS (Invitrogen) and 1× GlutaMAX (Invitrogen). One full 6-well tissue culture plate was seeded for each cell line used. Cells were allowed to adhere for 24 h before the induction of overexpression. For each cell line, 3 wells were treated with 1 μg/ml doxycycline (Dox+; Sigma) in DMSO or with DMSO (Dox−). Cells were incubated for 72 h postinduction before harvesting. Each well of HEK293 cells was harvested by treatment with 200 μl of TrypLE (Invitrogen). Detached cells were resuspended with 800 μl of DMEM + 10% FBS and cells. HEK293T cells were resuspended in 3 ml of culturing medium by pipetting. All cell samples were centrifuged at 1000 × *g* for 10 min to collect cells, and pellets were resuspended in ~250 μl of 1× PBS. Cells were counted by mixing a sample of the cell suspension with 0.4% trypan blue (Invitrogen) in a 1:1 ratio before counting on the Countess II cell counter (Invitrogen). For each sample, 100,000 viable cells were added to a 96-well white flat-bottomed plate (Nunclon). Two wells were plated for each sample: one for use with the $NADP^+$/NADPH Glo assay and one for use in the NADH/NAD^+ Glo assay (Promega), such that all four metabolites would be measured on the same plate for each set of samples. Relative amounts of each metabolite were measured according to the manufacturer's instructions. Briefly, each well was brought up to 50 μl of total volume with 1× PBS. Four wells of 1× PBS were added for blank measurements to each plate, one per metabolite. 50 μl of 1% dodecyltrimethylammonium bromide in 0.2 N NaOH was added to each well to lyse cells (base treatment). Fifty μl of the 100 μl cell suspension in base treatment was removed and added to an empty well. 25 μl of 0.4 N HCl was added to these samples (acid treatment). Plates were incubated at 60 °C for 15 min to selectively destroy the $NADP^+$/NAD^+ in the base treatment and the NADPH/NADH in the acid treatment. The samples were brought to room temperature before neutralization of the base solutions with 50 μl of 0.25 M Tris base + 0.2 N HCl and of the acid solutions with 25 μl of 0.5 M Tris base. All samples were in 100 μl of total volume at this point, with 50,000 cells/well. 50 μl of sample was removed from the wells measuring NADPH, NADH, and $NADP^+$, whereas 90 μl of volume was removed from the wells measuring NAD^+ so that samples could be diluted into the linear range for the assay. Wells used for NAD^+ measurements were brought back up to 50 μl of total volume by adding 40 μl of 1× PBS. Reconstituted $NADP^+$/NADPH Glo reagent was added to one set of acid- and base-treated wells, and reconstituted NAD^+/NADH Glo reagent was added to the other set of acid- and base-treated samples.

Plates were incubated at room temperature for 1 h before luminescence was measured using a GloMAX Discover plate reader luminometer (Promega). Three replicate experiments were performed with three biological replicates for each cell type and treatment within each experiment.

The metabolite assays were analyzed using Bayesian hierarchical models, following the same general approach as that outlined above for the analysis of RT-qPCR experiments and ATP measurements. We took as primary data the 0-centered $\log_2$ luminescence measurements output by the GloMAX assay and fitted a model with population-level effects for the cell line, metabolite of interest, condition (induced *versus* uninduced), and all possible interactions of those three features and group-level effects for the biological replicates. We assumed Student's *t* distributed errors, with a normal(0,5) prior on the population-level effects and brms default priors for all other parameters. The model was fitted and assessed as described above for the RT-qPCR data. Data and statistics values are reported in Table S2.

Data availability

RNA-Seq data are available at the Gene Expression Omnibus (GSE142749; RNA-Seq of HEK293 cells overexpressing NOCT Δ(2–15)-3F with controls overexpressing GST-3F). All other data are reported in the article and supporting information, including the following associated files. The supporting information file reports the minimum information for publication of quantitative real-time PCR experiments (MIQE) data. Table S1 that reports the RNA-Seq data and statistics for transcriptome analysis in response to overexpressed NOCTΔ(2–15)-3F in HEK293 cells. Table S2 provides data and statistics for graphs in Figs. 5 and 7. Table S3 presents those data and statistics pertaining to Figs. S5–S8.

Acknowledgments—We thank the members of the Goldstrohm, Freddolino, Trievel, and Rorbach laboratories for helpful suggestions and advice during the course of these studies. The Genotype-Tissue Expression (GTEx) Project was supported by the Common Fund of the Office of the Director of the National Institutes of Health and by NCI, NHGRI, NHLBI, NIDA, NIMH, and NINDS.

Author contributions—E. T. A., K. L. H., R. D., S. P., R. C. T., J. R., P. L. F., and A. C. G. conceptualization; E. T. A., R. D., and P. L. F. formal analysis; E. T. A., K. L. H., R. D., S. P., and S. G. investigation; E. T. A., K. L. H., R. D., S. P., S. G., J. R., P. L. F., and A. C. G. visualization; E. T. A., K. L. H., R. D., S. P., P. L. F., and A. C. G. methodology; E. T. A., K. L. H., R. D., S. P., S. G., R. C. T., J. R., P. L. F., and A. C. G. writing-original draft; E. T. A., R. C. T., J. R., P. L. F., and A. C. G. project administration; E. T. A., K. L. H., R. D., S. P., R. C. T., J. R., P. L. F., and A. C. G. writing-review and editing; R. C. T., J. R., P. L. F., and A. C. G. supervision; R. C. T., J. R., P. L. F., and A. C. G. funding acquisition; P. L. F. software.

Funding and additional information—This research was supported by funding from the Max Planck Institute, Karolinska Institutet, Marie Sklodowska Curie Actions International Career Grant 2015-00579, and Knut and Alice Wallenberg Foundation Grant WAF 2017 (to J. R.); NIGMS, National Institutes of Health, Grant R35 GM128637 (to P. F.); NIGMS, National Institutes of Health, Grant R01 GM105707 and an Edward Mallinckrodt Jr. Foundation Grant (to A. G.); a University of Michigan Nutrition and Obesity Research Center Pilot Grant through National Institutes of Health Grant DK089503 (to R. T.); and American Heart Association Predoctoral Fellowship 16PRE26700002 and Chemistry-Biology Training Program Fellowship 5T32GM008597 (to E. A.). Additional funding, including publication charges, was provided by the University of Minnesota. The content is solely the responsibility of the authors and does not necessarily represent the official views of the National Institutes of Health.

Conflict of interest—The authors declare that they have no conflicts of interest with the contents of this article.

Abbreviations—The abbreviations used are: NOCT, Nocturnin; rNOCT, recombinant NOCT; EEP, exonuclease-endonuclease-phosphatase; MTS, mitochondrial targeting sequence; aa, amino acids; TOM, translocase of outer membrane; 3F, 3×FLAG; MPP, mitochondrial processing peptidase; ERCC, External RNA Control Consortium; qPCR, quantitative PCR; GO, gene ontology; Dox, doxycycline; GAPDH, glyceraldehyde-3-phosphate dehydrogenase; PVDF, polyvinylidene difluoride; FBS, fetal bovine serum; DMEM, Dulbecco's modified Eagle's medium; mRIPA, modified radioimmunoprecipitation assay; HRP, horseradish peroxidase; VCL, vinculin; GST, glutathione *S*-transferase; FDR, false discovery rate; TPM, transcripts per million; EGFP, enhanced GFP.

References

1. Abshire, E. T., Chasseur, J., Bohn, J. A., Del Rizzo, P. A., Freddolino, P. L., Goldstrohm, A. C., and Trievel, R. C. (2018) The structure of human Nocturnin reveals a conserved ribonuclease domain that represses target transcript translation and abundance in cells. *Nucleic Acids Res.* **46,** 6257–6270 CrossRef Medline
2. Baggs, J. E., and Green, C. B. (2003) Nocturnin, a deadenylase in *Xenopus laevis* retina: a mechanism for posttranscriptional control of circadian-related mRNA. *Curr. Biol.* **13,** 189–198 CrossRef Medline
3. Blanco, A. M., Gomez-Boronat, M., Madera, D., Valenciano, A. I., Alonso-Gomez, A. L., and Delgado, M. J. (2017) First evidence of nocturnin in fish: two isoforms in goldfish differentially regulated by feeding. *Am. J. Physiol. Regul. Integr. Comp. Physiol.* **314,** R304–R312 CrossRef Medline
4. Green, C. B., Douris, N., Kojima, S., Strayer, C. A., Fogerty, J., Lourim, D., Keller, S. R., and Besharse, J. C. (2007) Loss of Nocturnin, a circadian deadenylase, confers resistance to hepatic steatosis and diet-induced obesity. *Proc. Natl. Acad. Sci. U. S. A.* **104,** 9888–9893 CrossRef Medline
5. Grönke, S., Bickmeyer, I., Wunderlich, R., Jäckle, H., and Kühnlein, R. P. (2009) Curled encodes the *Drosophila* homolog of the vertebrate circadian deadenylase Nocturnin. *Genetics* **183,** 219–232 CrossRef Medline
6. Hughes, K. L., Abshire, E. T., and Goldstrohm, A. C. (2018) Regulatory roles of vertebrate Nocturnin: insights and remaining mysteries. *RNA Biol.* **15,** 1255–1267 CrossRef Medline
7. Goldstrohm, A. C., and Wickens, M. (2008) Multifunctional deadenylase complexes diversify mRNA control. *Nat. Rev. Mol. Cell Biol.* **9,** 337–344 CrossRef Medline
8. Douris, N., Kojima, S., Pan, X., Lerch-Gaggl, A. F., Duong, S. Q., Hussain, M. M., and Green, C. B. (2011) Nocturnin regulates circadian trafficking of dietary lipid in intestinal enterocytes. *Curr. Biol.* **21,** 1347–1355 CrossRef Medline
9. Kawai, M., Green, C. B., Lecka-Czernik, B., Douris, N., Gilbert, M. R., Kojima, S., Ackert-Bicknell, C., Garg, N., Horowitz, M. C., Adamo, M. L., Clemmons, D. R., and Rosen, C. J. (2010) A circadian-regulated gene,

Nocturnin, promotes adipogenesis by stimulating PPAR-γ nuclear translocation. *Proc. Natl. Acad. Sci. U. S. A.* **107,** 10508–10513 CrossRef Medline
10. Kawai, M., Delany, A. M., Green, C. B., Adamo, M. L., and Rosen, C. J. (2010) Nocturnin suppresses igf1 expression in bone by targeting the 3' untranslated region of igf1 mRNA. *Endocrinology* **151,** 4861–4870 CrossRef Medline
11. Garbarino-Pico, E., Niu, S., Rollag, M. D., Strayer, C. A., Besharse, J. C., and Green, C. B. (2007) Immediate early response of the circadian polyA ribonuclease nocturnin to two extracellular stimuli. *RNA* **13,** 745–755 CrossRef Medline
12. Estrella, M. A., Du, J., and Korennykh, A. (2018) Crystal structure of human nocturnin catalytic domain. *Sci. Rep.* **8,** 16294 CrossRef Medline
13. Brown, J. A., Bulkley, D., Wang, J., Valenstein, M. L., Yario, T. A., Steitz, T. A., and Steitz, J. A. (2014) Structural insights into the stabilization of MALAT1 noncoding RNA by a bipartite triple helix. *Nat. Struct. Mol. Biol.* **21,** 633–640 CrossRef Medline
14. Wilusz, J. E., JnBaptiste, C. K., Lu, L. Y., Kuhn, C. D., Joshua-Tor, L., and Sharp, P. A. (2012) A triple helix stabilizes the 3' ends of long noncoding RNAs that lack poly(A) tails. *Genes Dev.* **26,** 2392–2407 CrossRef Medline
15. Cooke, A., Prigge, A., and Wickens, M. (2010) Translational repression by deadenylases. *J. Biol. Chem.* **285,** 28506–28513 CrossRef Medline
16. Waghray, S., Williams, C., Coon, J. J., and Wickens, M. (2015) *Xenopus* CAF1 requires NOT1-mediated interaction with 4E-T to repress translation *in vivo*. *RNA* **21,** 1335–1345 CrossRef Medline
17. Kojima, S., Gendreau, K. L., Sher-Chen, E. L., Gao, P., and Green, C. B. (2015) Changes in poly(A) tail length dynamics from the loss of the circadian deadenylase Nocturnin. *Sci. Rep.* **5,** 17059 CrossRef Medline
18. Stubblefield, J. J., Gao, P., Kilaru, G., Mukadam, B., Terrien, J., and Green, C. B. (2018) Temporal control of metabolic amplitude by nocturnin. *Cell Rep.* **22,** 1225–1235 CrossRef Medline
19. Hee, S. W., Tsai, S. H., Chang, Y. C., Chang, C. J., Yu, I. S., Lee, P. C., Lee, W. J., Yun-Chia Chang, E., and Chuang, L. M. (2012) The role of nocturnin in early adipogenesis and modulation of systemic insulin resistance in human. *Obesity* **20,** 1558–1565 CrossRef Medline
20. Onder, Y., Laothamatas, I., Berto, S., Sewart, K., Kilaru, G., Bordieanu, B., Stubblefield, J. J., Konopka, G., Mishra, P., and Green, C. B. (2019) The circadian protein nocturnin regulates metabolic adaptation in brown adipose tissue. *iScience* **19,** 83–92 CrossRef Medline
21. Pearce, S. F., Rorbach, J., Haute, L. V., D'Souza, A. R., Rebelo-Guiomar, P., Powell, C. A., Brierley, I., Firth, A. E., and Minczuk, M. (2017) Maturation of selected human mitochondrial tRNAs requires deadenylation. *Elife* **6,** CrossRef Medline
22. Rorbach, J., Nicholls, T. J., and Minczuk, M. (2011) PDE12 removes mitochondrial RNA poly(A) tails and controls translation in human mitochondria. *Nucleic Acids Res.* **39,** 7750–7763 CrossRef Medline
23. Wood, E. R., Bledsoe, R., Chai, J., Daka, P., Deng, H., Ding, Y., Harris-Gurley, S., Kryn, L. H., Nartey, E., Nichols, J., Nolte, R. T., Prabhu, N., Rise, C., Sheahan, T., Shotwell, J. B., *et al.* (2015) The role of phosphodiesterase 12 (PDE12) as a negative regulator of the innate immune response and the discovery of antiviral inhibitors. *J. Biol. Chem.* 290, 19681–19696 CrossRef Medline
24. Estrella, M. A., Du, J., Chen, L., Rath, S., Prangley, E., Chitrakar, A., Aoki, T., Schedl, P., Rabinowitz, J., and Korennykh, A. (2019) The metabolites $NADP^+$ and NADPH are the targets of the circadian protein Nocturnin (Curled). *Nat. Commun.* **10,** 2367 CrossRef Medline
25. Estrella, M. A., Du, J., Chen, L., Rath, S., Prangley, E., Chitrakar, A., Aoki, T., Schedl, P., Rabinowitz, J., and Korennykh, A. (2019) The metabolites $NADP^+$ and NADPH are the targets of the circadian protein Nocturnin (Curled). *Biorxiv* CrossRef CrossRef
26. Le, P. T., Bornstein, S. A., Motyl, K. J., Tian, L., Stubblefield, J. J., Hong, H. K., Takahashi, J. S., Green, C. B., Rosen, C. J., and Guntur, A. R. (2019) A novel mouse model overexpressing Nocturnin results in decreased fat mass in male mice. *J. Cell. Physiol.* **234,** 20228–20239 CrossRef
27. Kozak, M. (1991) Effects of long 5' leader sequences on initiation by eukaryotic ribosomes *in vitro*. *Gene Expr.* **1,** 117–125 Medline
28. Kozak, M. (1991) A short leader sequence impairs the fidelity of initiation by eukaryotic ribosomes. *Gene Expr.* **1,** 111–115
29. Aitken, C. E., and Lorsch, J. R. (2012) A mechanistic overview of translation initiation in eukaryotes. *Nat. Struct. Mol. Biol.* **19,** 568–576 CrossRef Medline
30. Benitez-Cantos, M. S., Yordanova, M. M., O'Connor, P. B. F., Zhdanov, A. V., Kovalchuk, S. I., Papkovsky, D. B., Andreev, D. E., and Baranov, P. V. (2020) Translation initiation downstream from annotated start codons in human mRNAs coevolves with the Kozak context. *Genome Res.* **30,** 974–984 CrossRef Medline
31. Fukasawa, Y., Tsuji, J., Fu, S. C., Tomii, K., Horton, P., and Imai, K. (2015) MitoFates: improved prediction of mitochondrial targeting sequences and their cleavage sites. *Mol. Cell. Proteomics* **14,** 1113–1126 CrossRef Medline
32. Savojardo, C., Martelli, P. L., Fariselli, P., and Casadio, R. (2014) TPpred2: improving the prediction of mitochondrial targeting peptide cleavage sites by exploiting sequence motifs. *Bioinformatics* **30,** 2973–2974 CrossRef Medline
33. Indio, V., Martelli, P. L., Savojardo, C., Fariselli, P., and Casadio, R. (2013) The prediction of organelle-targeting peptides in eukaryotic proteins with grammatical-restrained hidden conditional random fields. *Bioinformatics* **29,** 981–988 CrossRef Medline
34. Bauer, N. C., Doetsch, P. W., and Corbett, A. H. (2015) Mechanisms regulating protein localization. *Traffic* **16,** 1039–1061 CrossRef Medline
35. Shaw, G., Morse, S., Ararat, M., and Graham, F. L. (2002) Preferential transformation of human neuronal cells by human adenoviruses and the origin of HEK 293 cells. *FASEB J.* **16,** 869–871 CrossRef Medline
36. Lin, Y. C., Boone, M., Meuris, L., Lemmens, I., Van Roy, N., Soete, A., Reumers, J., Moisse, M., Plaisance, S., Drmanac, R., Chen, J., Speleman, F., Lambrechts, D., Van de Peer, Y., Tavernier, J., *et al.* (2014) Genome dynamics of the human embryonic kidney 293 lineage in response to cell biology manipulations. *Nat. Commun.* **5,** 4767 CrossRef Medline
37. Gilbert, M. R., Douris, N., Tongjai, S., and Green, C. B. (2011) Nocturnin expression is induced by fasting in the white adipose tissue of restricted fed mice. *PLoS One* **6,** e17051 CrossRef Medline
38. Li, R., Yue, J., Zhang, Y., Zhou, L., Hao, W., Yuan, J., Qiang, B., Ding, J. M., Peng, X., and Cao, J. M. (2008) CLOCK/BMAL1 regulates human nocturnin transcription through binding to the E-box of nocturnin promoter. *Mol. Cell. Biochem.* **317,** 169–177 CrossRef Medline
39. Rasmussen, A. H., Rasmussen, H. B., and Silahtaroglu, A. (2017) The DLGAP family: neuronal expression, function and role in brain disorders. *Mol. Brain* **10,** 43 CrossRef Medline
40. Byun, H., Lee, H. L., Liu, H., Forrest, D., Rudenko, A., and Kim, I. J. (2019) Rorbeta regulates selective axon-target innervation in the mammalian midbrain. *Development* **146,** dev171926 CrossRef Medline
41. Roforth, M. M., Liu, G., Khosla, S., and Monroe, D. G. (2012) Examination of nuclear receptor expression in osteoblasts reveals Rorβ as an important regulator of osteogenesis. *J. Bone Miner. Res.* **27,** 891–901 CrossRef Medline
42. Mo, H. Y., Jo, Y. S., Yoo, N. J., Kim, M. S., Song, S. Y., and Lee, S. H. (2019) Frameshift mutation of candidate tumor suppressor genes QK1 and TMEFF2 in gastric and colorectal cancers. *Cancer Biomark.* **24,** 1–6 CrossRef Medline
43. Xia, Z., Ouyang, D., Li, Q., Li, M., Zou, Q., Li, L., Yi, W., and Zhou, E. (2019) The expression, functions, interactions and prognostic values of PTPRZ1: a review and bioinformatic analysis. *J. Cancer* **10,** 1663–1674 CrossRef Medline
44. Madeo, M., Stewart, M., Sun, Y., Sahir, N., Wiethoff, S., Chandrasekar, I., Yarrow, A., Rosenfeld, J. A., Yang, Y., Cordeiro, D., McCormick, E. M., Muraresku, C. C., Jepperson, T. N., McBeth, L. J., Seidahmed, M. Z., *et al.* (2016) Loss-of-function mutations in FRRS1L lead to an epileptic-dyskinetic encephalopathy. *Am. J. Hum. Genet.* **98,** 1249–1255 CrossRef Medline
45. Schwenk, J., Boudkkazi, S., Kocylowski, M. K., Brechet, A., Zolles, G., Bus, T., Costa, K., Kollewe, A., Jordan, J., Bank, J., Bildl, W., Sprengel, R., Kulik, A., Roeper, J., Schulte, U., and Fakler, B. (2019) An ER assembly line of AMPA-receptors controls excitatory neurotransmission and its plasticity. *Neuron* **104,** 680–692.e9 CrossRef Medline

46. Goodarzi, H., Elemento, O., and Tavazoie, S. (2009) Revealing global regulatory perturbations across human cancers. *Mol. Cell* **36,** 900–911 CrossRef Medline
47. Guntur, A. R., Kawai, M., Le, P., Bouxsein, M. L., Bornstein, S., Green, C. B., and Rosen, C. J. (2011) An essential role for the circadian-regulated gene nocturnin in osteogenesis: the importance of local timekeeping in skeletal homeostasis. *Ann. N. Y. Acad. Sci.* **1237,** 58–63 CrossRef Medline
48. Lehman, A., Thouta, S., Mancini, G. M. S., Naidu, S., van Slegtenhorst, M., McWalter, K., Person, R., Mwenifumbo, J., Salvarinova, R., CAUSES Study, EPGEN Study, Guella, I., McKenzie, M. B., Datta, A., Connolly, M. B., *et al.* (2017) Loss-of-function and gain-of-function mutations in KCNQ5 cause intellectual disability or epileptic encephalopathy. *Am. J. Hum. Genet.* **101,** 65–74 CrossRef Medline
49. Niday, Z., Hawkins, V. E., Soh, H., Mulkey, D. K., and Tzingounis, A. V. (2017) Epilepsy-associated KCNQ2 channels regulate multiple intrinsic properties of layer 2/3 pyramidal neurons. *J. Neurosci.* **37,** 576–586 CrossRef Medline
50. Kazak, L., Reyes, A., Duncan, A. L., Rorbach, J., Wood, S. R., Brea-Calvo, G., Gammage, P. A., Robinson, A. J., Minczuk, M., and Holt, I. J. (2013) Alternative translation initiation augments the human mitochondrial proteome. *Nucleic Acids Res.* **41,** 2354–2369 CrossRef Medline
51. Kazak, L., Reyes, A., He, J., Wood, S. R., Brea-Calvo, G., Holen, T. T., and Holt, I. J. (2013) A cryptic targeting signal creates a mitochondrial FEN1 isoform with tailed R-loop binding properties. *PLoS One* **8,** e62340 CrossRef Medline
52. Lee, J., O'Neill, R. C., Park, M. W., Gravel, M., and Braun, P. E. (2006) Mitochondrial localization of CNP2 is regulated by phosphorylation of the N-terminal targeting signal by PKC: implications of a mitochondrial function for CNP2 in glial and non-glial cells. *Mol. Cell Neurosci.* **31,** 446–462 CrossRef Medline
53. Hornbeck, P. V., Zhang, B., Murray, B., Kornhauser, J. M., Latham, V., and Skrzypek, E. (2015) PhosphoSitePlus, 2014: mutations, PTMs and recalibrations. *Nucleic Acids Res.* **43,** D512–D520 CrossRef Medline
54. Pearce, S. F., Rebelo-Guiomar, P., D'Souza, A. R., Powell, C. A., Van Haute, L., and Minczuk, M. (2017) Regulation of mammalian mitochondrial gene expression: recent advances. *Trends Biochem. Sci.* **42,** 625–639 CrossRef Medline
55. D'Souza, A. R., and Minczuk, M. (2018) Mitochondrial transcription and translation: overview. *Essays Biochem.* **62,** 309–320 CrossRef Medline
56. Ying, W. (2008) NAD^+/NADH and $NADP^+$/NADPH in cellular functions and cell death: regulation and biological consequences. *Antioxid. Redox Signal.* **10,** 179–206 CrossRef Medline
57. Xiao, W., Wang, R. S., Handy, D. E., and Loscalzo, J. (2018) NAD(H) and NADP(H) redox couples and cellular energy metabolism. *Antioxid. Redox Signal.* **28,** 251–272 CrossRef Medline
58. Canto, C., Menzies, K. J., and Auwerx, J. (2015) NAD^+ metabolism and the control of energy homeostasis: a balancing act between mitochondria and the nucleus. *Cell Metab.* **22,** 31–53 CrossRef Medline
59. Nikiforov, A., Dölle, C., Niere, M., and Ziegler, M. (2011) Pathways and subcellular compartmentation of NAD biosynthesis in human cells: from entry of extracellular precursors to mitochondrial NAD generation. *J. Biol. Chem.* **286,** 21767–21778 CrossRef Medline
60. Adler, L. T., Chen, C., and Koutalos, Y. (2014) Mitochondria contribute to NADPH generation in mouse rod photoreceptors. *J. Biol. Chem.* **289,** 1519–1528 CrossRef Medline
61. Davila, A., Liu, L., Chellappa, K., Redpath, P., Nakamaru-Ogiso, E., Paolella, L. M., Zhang, Z. G., Migaud, M. E., Rabinowitz, J. D., and Baur, J. A. (2018) Nicotinamide adenine dinucleotide is transported into mammalian mitochondria. *Elife* **7,** e33246 CrossRef Medline
62. Brooks, G. A. (2018) The science and translation of lactate shuttle theory. *Cell Metab.* **27,** 757–785 CrossRef Medline
63. Ohashi, K., Kawai, S., and Murata, K. (2012) Identification and characterization of a human mitochondrial NAD kinase. *Nat. Commun.* **3,** 1248 CrossRef Medline
64. Kawai, S., and Murata, K. (2008) Structure and function of NAD kinase and NADP phosphatase: key enzymes that regulate the intracellular balance of NAD(H) and NADP(H). *Biosci. Biotechnol. Biochem.* **72,** 919–930 CrossRef Medline
65. Ding, C. C., Rose, J., Sun, T., Wu, J., Chen, P. H., Lin, C. C., Yang, W. H., Chen, K. Y., Lee, H., Xu, E., Tian, S., Akinwuntan, J., Zhao, J., Guan, Z., Zhou, P., *et al.* (2020) MESH1 is a cytosolic NADPH phosphatase that regulates ferroptosis. *Nat. Metab.* **2,** 270–277 CrossRef Medline
66. Hentze, M. W., Caughman, S. W., Rouault, T. A., Barriocanal, J. G., Dancis, A., Harford, J. B., and Klausner, R. D. (1987) Identification of the iron-responsive element for the translational regulation of human ferritin mRNA. *Science* **238,** 1570–1573 CrossRef Medline
67. Muckenthaler, M., Gray, N. K., and Hentze, M. W. (1998) IRP-1 binding to ferritin mRNA prevents the recruitment of the small ribosomal subunit by the cap-binding complex eIF4F. *Mol. Cell* **2,** 383–388 CrossRef Medline
68. Müllner, E. W., Rothenberger, S., Müller, A. M., and Kühn, L. C. (1992) *In vivo* and *in vitro* modulation of the mRNA-binding activity of iron-regulatory factor: tissue distribution and effects of cell proliferation, iron levels and redox state. *Eur. J. Biochem.* **208,** 597–605 CrossRef Medline
69. Constable, A., Quick, S., Gray, N. K., and Hentze, M. W. (1992) Modulation of the RNA-binding activity of a regulatory protein by iron *in vitro*: switching between enzymatic and genetic function? *Proc. Natl. Acad. Sci. U. S. A.* **89,** 4554–4558 CrossRef Medline
70. Castello, A., Hentze, M. W., and Preiss, T. (2015) Metabolic enzymes enjoying new partnerships as RNA-binding proteins. *Trends Endocrinol. Metab.* **26,** 746–757 CrossRef Medline
71. Dollenmaier, G., and Weitz, M. (2003) Interaction of glyceraldehyde-3-phosphate dehydrogenase with secondary and tertiary RNA structural elements of the hepatitis A virus 3' translated and non-translated regions. *J. Gen. Virol.* **84,** 403–414 CrossRef Medline
72. Nagy, E., Henics, T., Eckert, M., Miseta, A., Lightowlers, R. N., and Kellermayer, M. (2000) Identification of the NAD^+-binding fold of glyceraldehyde-3-phosphate dehydrogenase as a novel RNA-binding domain. *Biochem. Biophys. Res. Commun.* **275,** 253–260 CrossRef Medline
73. Nagy, E., and Rigby, W. F. (1995) Glyceraldehyde-3-phosphate dehydrogenase selectively binds AU-rich RNA in the NAD^+-binding region (Rossmann fold). *J. Biol. Chem.* **270,** 2755–2763 CrossRef Medline
74. Minczuk, M., Piwowarski, J., Papworth, M. A., Awiszus, K., Schalinski, S., Dziembowski, A., Dmochowska, A., Bartnik, E., Tokatlidis, K., Stepien, P. P., and Borowski, P. (2002) Localisation of the human hSuv3p helicase in the mitochondrial matrix and its preferential unwinding of dsDNA. *Nucleic Acids Res.* **30,** 5074–5086 CrossRef Medline
75. Andrews, S., Krueger, F., Segonds-Pichonn, A., Biggins, L., Krueger, C., and Wingett, S. (2010) FastQC: A Quality Control Tool for High Throughput Sequence Data, Babraham Institute, Babraham, UK
76. Ewels, P., Magnusson, M., Lundin, S., and Käller, M. (2016) MultiQC: summarize analysis results for multiple tools and samples in a single report. *Bioinformatics* **32,** 3047–3048 CrossRef Medline
77. Martin, M. (2011) Cutadapt removes adapter sequences from high-throughput sequencing reads. *EMBnet.journal* **17,** 10 CrossRef
78. Bolger, A. M., Lohse, M., and Usadel, B. (2014) Trimmomatic: a flexible trimmer for Illumina sequence data. *Bioinformatics* **30,** 2114–2120 CrossRef Medline
79. Dobin, A., Davis, C. A., Schlesinger, F., Drenkow, J., Zaleski, C., Jha, S., Batut, P., Chaisson, M., and Gingeras, T. R. (2013) STAR: ultrafast universal RNA-seq aligner. *Bioinformatics* **29,** 15–21 CrossRef Medline
80. Li, H., Handsaker, B., Wysoker, A., Fennell, T., Ruan, J., Homer, N., Marth, G., Abecasis, G., Durbin, R., and 1000 Genome Project Data Processing Subgroup, (2009) The sequence alignment/map format and SAMtools. *Bioinformatics* **25,** 2078–2079 CrossRef Medline
81. Anders, S., Pyl, P. T., and Huber, W. (2015) HTSeq—a Python framework to work with high-throughput sequencing data. *Bioinformatics* **31,** 166–169 CrossRef Medline
82. Love, M. I., Huber, W., and Anders, S. (2014) Moderated estimation of fold change and dispersion for RNA-seq data with DESeq2. *Genome Biol.* **15,** 550 CrossRef Medline
83. Bourgon, R., Gentleman, R., and Huber, W. (2010) Independent filtering increases detection power for high-throughput experiments. *Proc. Natl. Acad. Sci. U. S. A.* **107,** 9546–9551 CrossRef Medline
84. Pagliarini, D. J., Calvo, S. E., Chang, B., Sheth, S. A., Vafai, S. B., Ong, S. E., Walford, G. A., Sugiana, C., Boneh, A., Chen, W. K., Hill, D. E., Vidal, M.,

Evans, J. G., Thorburn, D. R., Carr, S. A., *et al.* (2008) A mitochondrial protein compendium elucidates complex I disease biology. *Cell* **134,** 112–123 CrossRef Medline

85. Calvo, S. E., Clauser, K. R., and Mootha, V. K. (2016) MitoCarta2.0: an updated inventory of mammalian mitochondrial proteins. *Nucleic Acids Res.* **44,** D1251–D1257 CrossRef Medline
86. Durinck, S., Moreau, Y., Kasprzyk, A., Davis, S., De Moor, B., Brazma, A., and Huber, W. (2005) BioMart and Bioconductor: a powerful link between biological databases and microarray data analysis. *Bioinformatics* **21,** 3439–3440 CrossRef Medline
87. Ashburner, M., Ball, C. A., Blake, J. A., Botstein, D., Butler, H., Cherry, J. M., Davis, A. P., Dolinski, K., Dwight, S. S., Eppig, J. T., Harris, M. A., Hill, D. P., Issel-Tarver, L., Kasarskis, A., Lewis, S., *et al.* (2000) Gene ontology: tool for the unification of biology. The Gene Ontology Consortium. *Nat. Genet.* **25,** 25–29 CrossRef Medline
88. The Gene Ontology Consortium (2019) The Gene Ontology resource: 20 years and still GOing strong. *Nucleic Acids Res.* **47,** D330–D338 CrossRef Medline
89. Zerbino, D. R., Achuthan, P., Akanni, W., Amode, M. R., Barrell, D., Bhai, J., Billis, K., Cummins, C., Gall, A., Girón, C. G., Gil, L., Gordon, L., Haggerty, L., Haskell, E., Hourlier, T., *et al.* (2018) Ensembl 2018. *Nucleic Acids Res.* **46,** D754–D761 CrossRef Medline
90. Durinck, S., Spellman, P. T., Birney, E., and Huber, W. (2009) Mapping identifiers for the integration of genomic datasets with the R/Bioconductor package biomaRt. *Nat. Protoc.* **4,** 1184–1191 CrossRef Medline
91. Bürkner, P.-C. (2017) brms: an R package for Bayesian multilevel models using Stan. *J. Stat. Softw.* **80,** 28 CrossRef
92. Carpenter, B., Gelman, A., Hoffman, M. D., Lee, D., Goodrich, B., Betancourt, M., Brubaker, M., Guo, J., Li, P., and Riddell, A. (2017) Stan: a probabilistic programming language. *J. Stat. Softw.* **76,** 32
93. Bürkner, P.-C. (2018) Advanced Bayesian multilevel modeling with the R package brms. *R J.* **10,** 395–411 CrossRef
94. Arvola, R. M., Chang, C. T., Buytendorp, J. P., Levdansky, Y., Valkov, E., Freddolino, P. L., and Goldstrohm, A. C. (2020) Unique repression domains of Pumilio utilize deadenylation and decapping factors to accelerate destruction of target mRNAs. *Nucleic Acids Res.* **48,** 1843–1871 CrossRef Medline
95. Ganger, M. T., Dietz, G. D., and Ewing, S. J. (2017) A common base method for analysis of qPCR data and the application of simple blocking in qPCR experiments. *BMC Bioinformatics* **18,** 534 CrossRef Medline